e-JSNM

e-JURNAL SAINS NUKLEAR MALAYSIA

e-NUCLEAR SCIENCE JOURNAL OF MALAYSIA

Volume 37 (No.2) 2025

A scientific journal by Malaysian Nuclear Agency

eISSN 2232-0946

eJURNAL
SAINS NUKLEAR MALAYSIA
VOL. 37 NO. 2 (2025)
eISSN: 2232-0946

Jurnal Sains Nuklear Malaysia (JSNM, Nuclear Science Journal of Malaysia) is published in the months of June and December annually since 1982 by the Malaysian Nuclear Agency (formerly known as PUSPATI, UTN and MINT). This journal provides a platform for researchers, scientists and engineers (RSEs) to publish their research findings and reviews related to nuclear science and technology so that they can be shared with colleagues throughout the world.

As a means to internationalise JSNM, the Board of Editors welcomes scientific, technical and review articles written by members of the scientific community from home and abroad.

Previously a purely traditional printed journal, JSNM is now adapted and available in electronic form, in keeping with demands and rapid development of ICT. This adaptation also translates to ease of accessibility of JSNM for scientific communities as well as to facilitate knowledge sharing among RSEs.

On behalf of the Editorial Board of JSNM, we would like to acknowledge and thank the authors and referees for their significant contributions to the success of this journal and for embracing this new publication format.

Every effort has been made to trace and acknowledge all copyright holders, but if any have been inadvertently overlooked, the publishers would please to make the necessary arrangements at the first opportunity.

Publishing Office
Malaysian Nuclear Agency, Bangi,
43000 Kajang,
Selangor Darul Ehsan,
MALAYSIA
Tel : +6 03 8911 2000
Fax : +6 03 8911 2154

Website
http://jsnm.nuclearmalaysia.gov.my

TABLE OF CONTENTS

Jurnal Sains Nuklear Malaysia, 2025, 37(No. 2): 1 – 19
ISSN: 2232-0946

PRELIMINARY CORE NEUTRONICS DESIGN FOR THE MALAYSIAN MPR BASED ON THE 30MW$_{TH}$ HANARO REACTOR

Mohamad Hairie Rabir*, Norfarizan Mohd Said, Mark Dennis Usang, Abi Muttaqin Jalal Bayar, Na'im Syauqi Hamzah, Phongsakorn Prak Tom, Hasniyati Md Razi, Muhammad Khairul Ariff Mustafa and Julia Abdul Karim

Reactor Technology Centre, Technical Support Division, Malaysian Nuclear Agency, Bangi, 43000 Kajang, Selangor, Malaysia
*Corresponding author: m_hairie@nm.gov.my

ABSTRACT

This paper presents a benchmarking study of the 30 MWth South Korean HANARO reactor to provide reference data for future conceptual studies of a Malaysian Multi-Purpose Research Reactor (MPR). The analysis, performed using the MCNPX 2.7 Monte Carlo radiation transport code, involved constructing a detailed HANARO core model and simulating key neutronic behavior, including criticality, neutron flux distribution, and fuel burnup. Simulation results were rigorously validated against experimental measurements at various irradiation sites, showing strong agreement for thermal neutron flux values and demonstrating the accuracy of the model in capturing core physics, non-uniform power distribution, and the effects of the heavy water reflector on thermal flux. These results establish a robust technical benchmark and a validated modeling approach that can inform preliminary core design considerations for a potential Malaysian MPR, which remains at the conceptual stage with no design decisions finalized. The study confirms that MCNPX 2.7 is a reliable tool for research reactor neutronics analysis and provides essential insights for future design and safety studies.

Keywords: Multi-Purpose Research Reactor (MPR), Neutronics Design, HANARO, MCNPX

INTRODUCTION

The Multi-Purpose Research Reactor (MPR) would serve as a versatile platform for advanced applications, including radioisotope production, high-quality irradiation, and experimental testing in the fields of medicine, agriculture, industry, and environmental research (MOSTI, 2023). The Malaysian Nuclear Agency (Nuklear Malaysia) is positioned to provide the technical foundation for a potential Multi-Purpose Research Reactor (MPR), which remains at the conceptual stage with no final design decisions made. Nuklear Malaysia's efforts focus on neutronics analysis, core modeling, and safety assessment, using validated computational tools and benchmarking against reference reactors such as HANARO. The team has developed detailed models, simulated reactor behavior, and explored fuel and irradiation configurations to generate essential scientific and engineering data. These preparatory studies establish a knowledge base to guide future MPR planning and align with the objectives of the Dasar Teknologi Nuklear Negara (DTNN) 2030.

In this study, several international reactor types were evaluated, including the VVR-TS (Russia), CARR (China), OPAL (Australia), and TRIGA (USA). The HANARO (High-flux Advanced Neutron Application Reactor) in South Korea was chosen as the primary reference due to its proven capabilities and high-power characteristics. The HANARO is an open-pool,

light-water cooled reactor with a thermal power of 30 MWth and a maximum thermal neutron flux of reaching up to 5.0×10^{14} n/cm²s in its flux trap. Its design incorporates an inverse neutron trap and a heavy water (D2O) reflector, which is highly efficient at slowing down fast neutrons and boosting the thermal flux in surrounding irradiation channels. The use of low-enriched uranium (LEU) fuel further aligns the design with global non-proliferation standards (Chae, et al., 1996).

This paper presents the preliminary conceptual neutronic design of the proposed Malaysian MPR, using the well-established HANARO reactor as a benchmark. The analysis was performed with the MCNPX 2.7 Monte Carlo radiation transport code. The primary goal is to develop a comprehensive neutronic model and validate its predictions against available operational and experimental HANARO data, providing a reliable technical foundation for Malaysia's future MPR. Without a validated neutronic model, optimizing the core for its intended purposes and ensuring compliance with international safety standards would not be possible. HANARO's extensive dataset serves as an essential reference for model validation. The specific objectives of this study are: (1) to develop a detailed three-dimensional MCNPX model of the HANARO reactor core, including geometry, materials, and irradiation facilities; (2) to simulate and analyze neutronic behavior, including effective multiplication factor (k_{eff}), thermal and fast neutron flux distribution, fuel burnup, and power density distribution; (3) to validate the model against experimental HANARO data; and (4) to provide a benchmarked technical basis to guide the design of the Malaysian MPR.

METHODOLOGY

Monte Carlo radiation transport code MCNPX 2.7 is well-suited for validation and equipped with several versatile tool for criticality, flux, burnup, and safety studies. MCNPX 2.7, developed by Los Alamos National Laboratory, supports neutron, photon, electron, and coupled transport, and uses extensive nuclear data libraries (ENDF7). It is proven and benchmarked for research reactor studies and is accepted by the international community (IAEA, OECD/NEA) (Goorlet et al. 2011).

The focus of the methodology is involved developing a detailed three-dimensional model of the reactor core. The model was meticulously constructed to represent the reactor's key components, including the pool (H_2O, R=200cm), reflector (D_2O, R=100cm, H=120cm), and fuel assemblies (H=70cm). The fuel assemblies were modelled as both 36-rod hexagonal and 18-rod cylindrical types standards (Chae, et al., 1996). The model also included various irradiation holes such as for the Neutron Transmutation Doping (NTD).

Figure 1 shows the MCNPX model illustrated in two perspectives: a top-down view (a) and a side view (b). The top-down view highlights the cylindrical geometry of the reactor core and its surrounding components. The outermost red region represents water in the pool, labelled as *Pool (H_2O)*. Concentric within this pool is a blue cylindrical region, corresponding to the reflector that surrounds the core. The reactor core itself, composed of numerous several coloured cylinders that represent different fuel elements and core components. Several white dots are also visible within the reflector, which correspond to irradiation channels.

To provide a clear overview of the physical and operational parameters used in the model, a summary of the core and fuel design characteristics is presented in Table 1. This table details key parameters such as the thermal power, coolant, reflector, fuel material, and the geometry

of the core. It also lists the dimensions of the fuel assemblies and the cycle length of the reactor's operation. In the reactor core model, the fuel is made up of two types of rods: standard and reduced. The standard rods, with a diameter of about 6.35 mm, are positioned in the inner sections of the fuel assemblies. Surrounding them are the reduced rods, which have a slightly smaller diameter of about 5.49 mm. This design helps improve neutron moderation in the outer regions of the core and contributes to a more even power distribution across the assemblies.

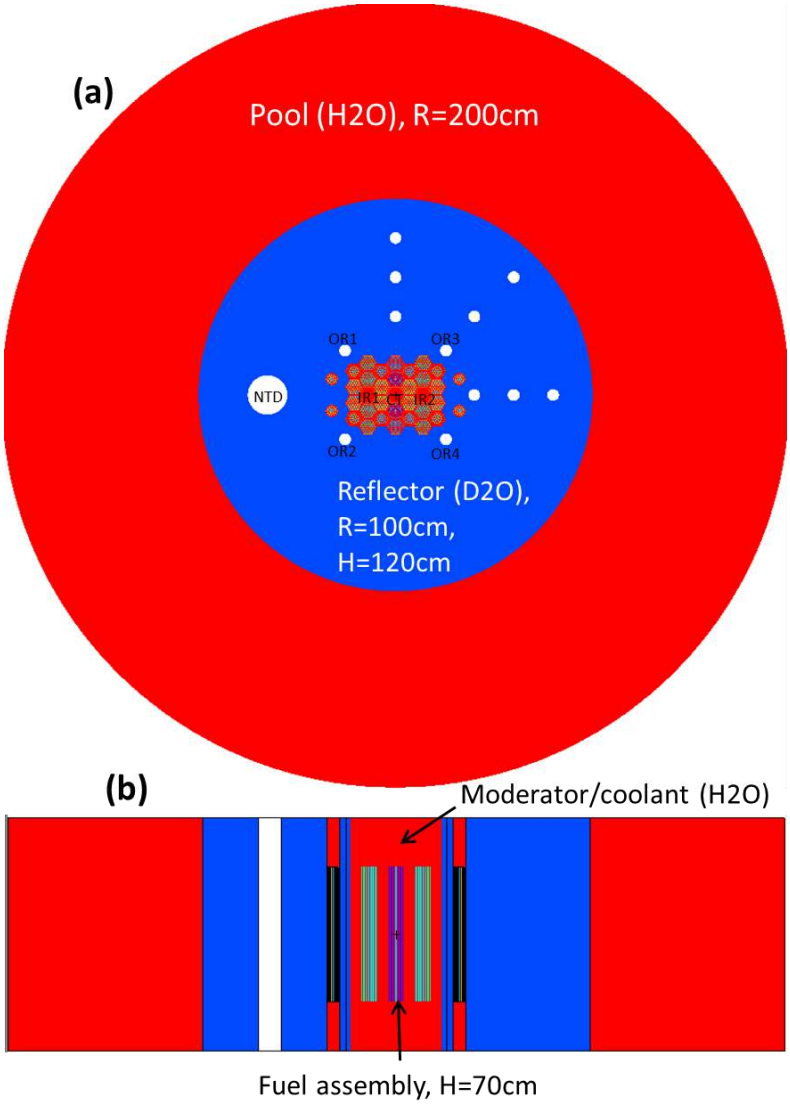

Figure 1. MCNPX model based on the HANARO reactor core shown in (a) top and (b) side views.

Table 1: Design and Operation Parameters [2]

Parameter	Value
	Reactor
Type	Open-tank-in-pool, 30 MW
Coolant/ Moderator	Light water (H2O)
Reflector	Heavy water (D2O)
Control Rods	Hafnium
	Core
Geometry	Hybrid type, 32 fuel assemblies
Reflector Dimensions	2.0 m diameter, 1.2 m height
Fuel Assembly Pitch	8.01 cm
	Fuel Rods
Fuel Material	Uranium silicide (U_3Si) dispersion
Enrichment	19.75% U−235
Cladding	Aluminum alloy (AA-1060)
Fuel Length	700 mm
Fuel Meat Diameter	6.35 mm (standard), 5.486 mm (reduced)
	Operation
Core Residence Time	~175 full-power days (~6 cycles)
Average Burnup	>50% U−235
Operating Cycle	28 days operation, 14 days maintenance

The referred HANARO reactor core provides high neutron fluxes across different irradiation sites. In the central trap (CT), the peak thermal neutron flux reaches 4.39×10^{14} n·cm^{-2}·s^{-1}, with a corresponding fast flux of 2.10×10^{14} n·cm^{-2}·s^{-1}. The inner irradiation region (IR) records slightly lower values, with thermal and fast fluxes of 3.93×10^{14} and 1.95×10^{14} n·cm^{-2}·s^{-1}, respectively. At the neutron transmutation doping (NTD) facility, the thermal flux is 6.20×10^{13} n·cm^{-2}·s^{-1} while the fast flux is much lower, at 1.11×10^{11} n·cm^{-2}·s^{-1}. In the outer irradiation region (OR), the thermal flux is 3.06×10^{14} n·cm^{-2}·s^{-1}, accompanied by a fast flux of 2.13×10^{13} n·cm^{-2}·s^{-1} (standards (Chae, et al., 1996; Kim, et al., 2016). These reference flux values serve as benchmark experimental data that will be used to compare and validate the MCNPX model results.

For the core model U_3Si–Al dispersion fuel meat, the bulk density is about 5.25 g/cm^3, with uranium contributing 3.15 g/cm^3. Assuming 19.75% enrichment in U-235 (balance U-238, neglecting U-234), the composition per cubic centimetre can be expressed as follows: U-235 accounts for 0.622 g (1.59×10^{21} atoms/cm^3), U-238 for 2.53 g (6.40×10^{21} atoms/cm^3), silicon

from the U_3Si phase for 0.124 g (2.66×10^{21} atoms/cm³), and aluminium for 1.98 g (4.42×10^{22} atoms/cm³). In terms of atom fractions, these correspond to 0.029 for U-235, 0.117 for U-238, 0.048 for Si, and 0.806 for Al, summing to unity within rounding. This representation provides the necessary basis for MCNP fuel definition using either atom fractions or atomic densities.

Figure 2 provides a detailed, zoomed-in view of the core model developed, highlighting the geometry and key components of the core. In the active core region (a), the central multi-colored section represents the reactor core, which contains both hexagonal and circular channels that house the fuel assemblies. The hexagonal fuel assemblies, together with the cylindrical assemblies, are arranged in a honeycomb-like configuration. White hexagonal spaces are reserved for experimental facilities, while the surrounding blue region denotes the heavy water reflector.

Panel (b) focuses on the details of the fuel assemblies and rods. On the left is a vertical cross-section of a fuel assembly showing individual rods with an active length of approximately 700 mm, while the right side provides a horizontal cross-section illustrating rod arrangements. The hexagonal assembly contains 36 rods in a hexagonal lattice, and the cylindrical assembly has 18 rods arranged in two concentric rings. The red background corresponds to the light water coolant, which flows through the assemblies to remove heat from the core.

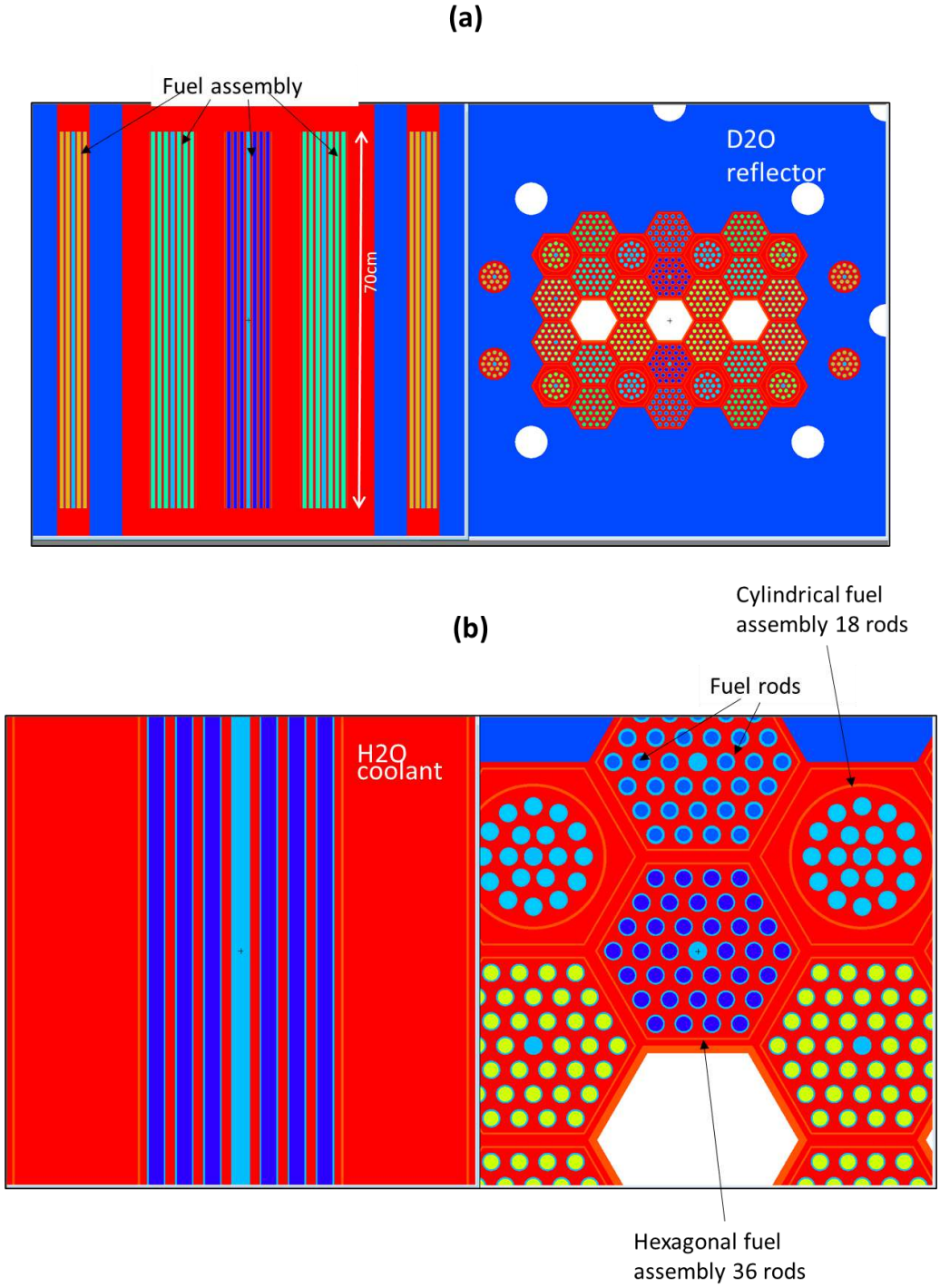

Figure 2. MCNP model of the core, fuel assemblies and rods.

A series of key neutronic parameters were calculated to characterize the reactor's behavior. The k_{eff} was determined using MCNPX's KCODE mode, which simulates successive neutron generations. The neutron flux (ϕ) tallies were obtained via the track length estimator (F4 tally), which measures the total path length of neutrons in a cell and normalizes it by the cell volume and number of source particles. These calculations provided detailed maps of neutron flux across the core, reflector, and irradiation channels.

To obtain absolute quantities and relate the MCNP results to the reactor's actual power level, a specific scaling procedure was implemented. Initialy, the average energy release per fission (E_f) was computed, which is approximately 200 MeV or 3.204×10^{-11} J. This value was used to calculate the fission rate (R_f) necessary to achieve the target power (P) of 30 MWth using the formula $R_f=P/E_f$. The MCNP tallies, which are initially given per one source neutron, were then scaled to match this required fission rate to obtain absolute quantities like absolute flux and absolute power density (Los Alamos National Laboratory, 2011). This method ensures that the simulation accurately reflects the physical conditions of a 30 MWth reactor. All MCNPX calculations were performed using the 'KCODE' card and an additional 'BURN' card for burnup analysis. To ensure statistical reliability, the error for k_{eff} results was kept below 0.00030, while the error for both the flux and mesh tallies was maintained below 5% by adjusting the particle history and the number of cycles.

Finally, the burnup of the fuel was simulated to understand the long-term behavior of the core over its operational cycle. The analysis considered the typical HANARO operational cycle of 28 days on followed by 14 days off for maintenance and refuelling (Shin, 2023). The simulations captured the effects of fuel depletion and the accumulation of fission products, highlighting the temporary reactivity reduction due to xenon poisoning at the start of each operational cycle. This time-dependent behavior provides essential information for fuel management and predicting the reactor core's end-of-life. Nevertheless, it should be noted that the observed power and reactivity variations are driven solely by changes in the burnup input in the MCNPX burn card, as actual control rod movements were not included in the model.

RESULTS AND DISCUSSION

Multiplication factor and burnup

Figure 3 visually represents the simulated operational characteristics of the MCNPX model over an irradiation campaign spanning approximately 250 days, detailing the reactor power history, neutron multiplication factor (k_{eff}), average core burnup, and U-235 depletion. This simulation provides a dynamic representation of the reactor's performance under realistic operating conditions, benchmarked against the established HANARO research reactor. The burnup calculations were performed using the MCNPX Tier-3 depletion option, which tracks the full inventory including fission products such as Xenon and Samarium. The time-dependent power history for a typical cycle was modeled using variable step durations: 1-day steps at the beginning of the cycle to capture rapid reactivity changes, 2-day and 4-day steps during intermediate periods, and 7-day steps for the remaining cycle to efficiently model long-term isotopic evolution. This sequence of time steps was repeated for a total of six operational cycles, allowing accurate simulation of fuel depletion, fission product buildup, and associated reactivity effects over extended operation.

Plot (a) illustrates the prescribed power schedule at operating mode of HANARO, it is a crucial input in this study that precisely mimics the 28-day full-power operation interspersed with 14-day zero-power intervals. This stepwise power profile is essential for accurately simulating transient phenomena, particularly the build-up and decay of fission product poisons such as Xe-135, power-dependent thermal-hydraulic reactivity feedbacks, and the cumulative fuel depletion. Plot (b), depicting the evolution of k_{eff}, exhibits two primary features: a monotonic downward trend and superimposed sawtooth oscillations. The long-term decline is a direct consequence of the progressive destruction of fissile material (U-235) and the accumulation of

non-fissile fission products (e.g., samarium-149 and stable isotopes), both of which introduce negative reactivity. The characteristic sawtooth oscillations are generated by the Xe-135 transient; during the 28-day power-up period, Xe-135 builds up to its equilibrium concentration, suppressing k_{eff}. During the subsequent 14-day zero-power shutdown, the Xe-135 rapidly decays, leading to the sharp increase (or 'sawtooth') in k_{eff} at the start of each new cycle.

The long-term performance indicators, Plots (c) and (d), provide critical metrics for fuel management. Plot (c) presents the average core burnup, expressed in GWd/MTU (Gigawatt-days per Metric Ton of Uranium). The plot shows a clear incremental increase only during the 28-day full-power phases, plateauing during the shutdown periods. The final predicted average burnup of approximately 98–99 GWd/MTU aligns remarkably well with reported discharge burnup data from HANARO (Chae et al., 2018). This correspondence strongly suggests that the MCNPX model accurately simulates the rate of energy extraction from the fuel. Plot (d) shows the depletion of U-235 over time, which is intrinsically linked to burnup accumulation. The simulated final depletion level approaches ~60%, which is quantitatively comparable to the 59.1% U-235 depletion values reported from extended irradiation experiments in the reference reactor (Chae et al., 2018). Interestingly, the simulation demonstrates that k_{eff} gradually decreases to nearly 1.0 after about six operating cycles (approximately 175 full-power days, 6×28 days), which correlates well with HANARO's typical fuel residence time before full discharge.

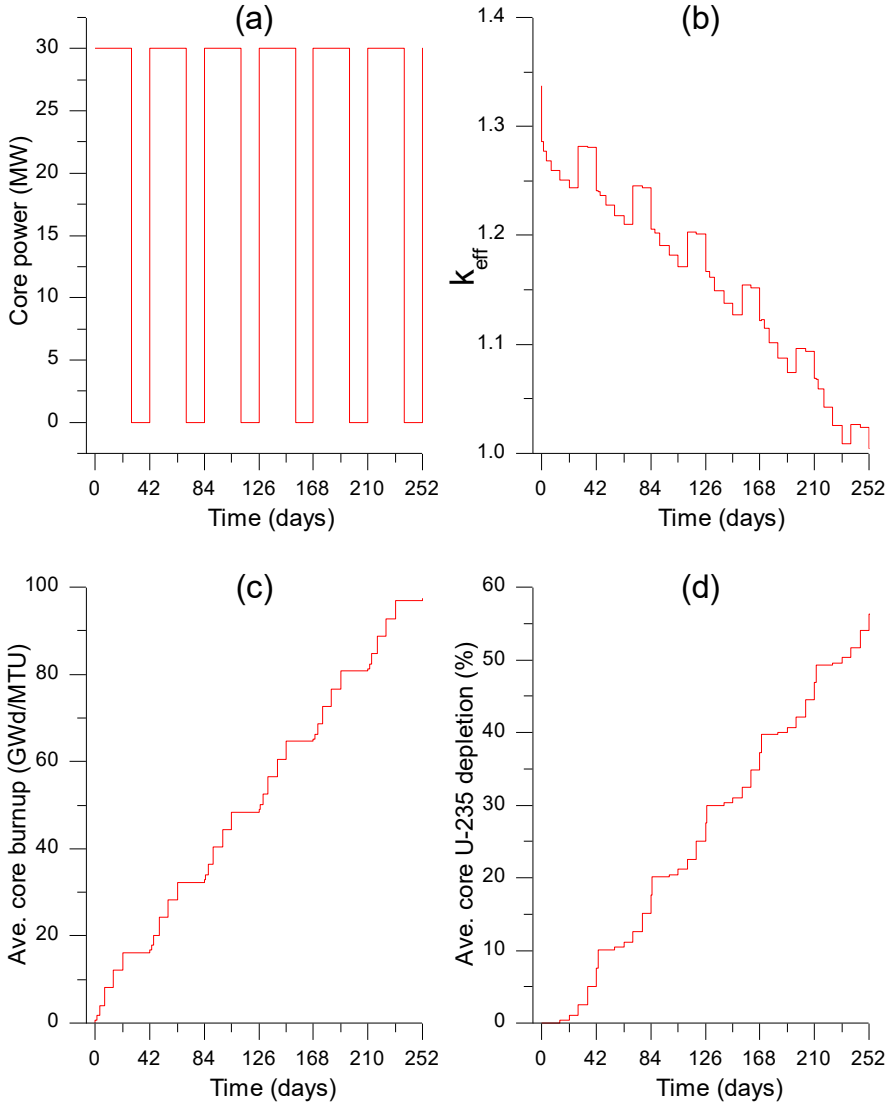

Figure 3. Simulated HANARO operation showing (a) power history, (b) k_{eff} trend, (c) burnup progression, and (d) U-235 depletion.

Neutron flux distribution

Comparison of neutron flux distributions is crucial because flux represents the spatially and energy-resolved parameter that directly controls irradiation conditions, material testing environments, and isotopic evolution. While k_{eff} and burnup validate overall reactor behavior, flux validation confirms the model can accurately reproduce the local neutron field in both magnitude and spectrum, which is vital for reliably predicting reaction rates, radionuclide inventories, and the effective use of irradiation facilities. Figure 4 presents this validation, detailing a comparison of neutron fluxes predicted by the MCNPX model against measured HANARO data at four key irradiation facilities—CT, IR, NTD, and OR—across two energy ranges: thermal (<0.625 eV) and fast (>0.82 MeV) (Chae et al., 1996). For the thermal flux distribution, the MCNPX simulation shows excellent agreement in the core-adjacent regions (CT and IR), which exhibit the highest flux levels (~10^{14} n·cm^2.s^{-1}), with differences of less than 3%. However, larger deviations occur in the moderated regions: the calculated thermal flux overestimates the NTD data by nearly 50%, while it underestimates the OR data by over

26%. For the fast neutron flux distribution, a similarly good agreement is observed in the high-flux regions (CT and IR), though the model's precision is slightly lower, with differences ranging from -10% to nearly -30%. In the moderated regions, the discrepancies are more pronounced, as the modeled fast flux at the NTD location, approximately five times higher approximately 6.23E11 in the model and 1.11E11 in the HANARO. The larger deviations can be attributed to uncertainties in the irradiation facility model, particularly in the geometric representation and the exact positioning of the irradiation channels. In most facilities, such as the NTD, the precise design details and actual locations of the channels are not publicly available. Consequently, the MCNPX model must rely on assumed or approximate positions and simplified geometries, which can introduce disscrepancies between calculated and measured neutron fluxes, especially in regions sensitive to local heterogeneities or shielding effects.

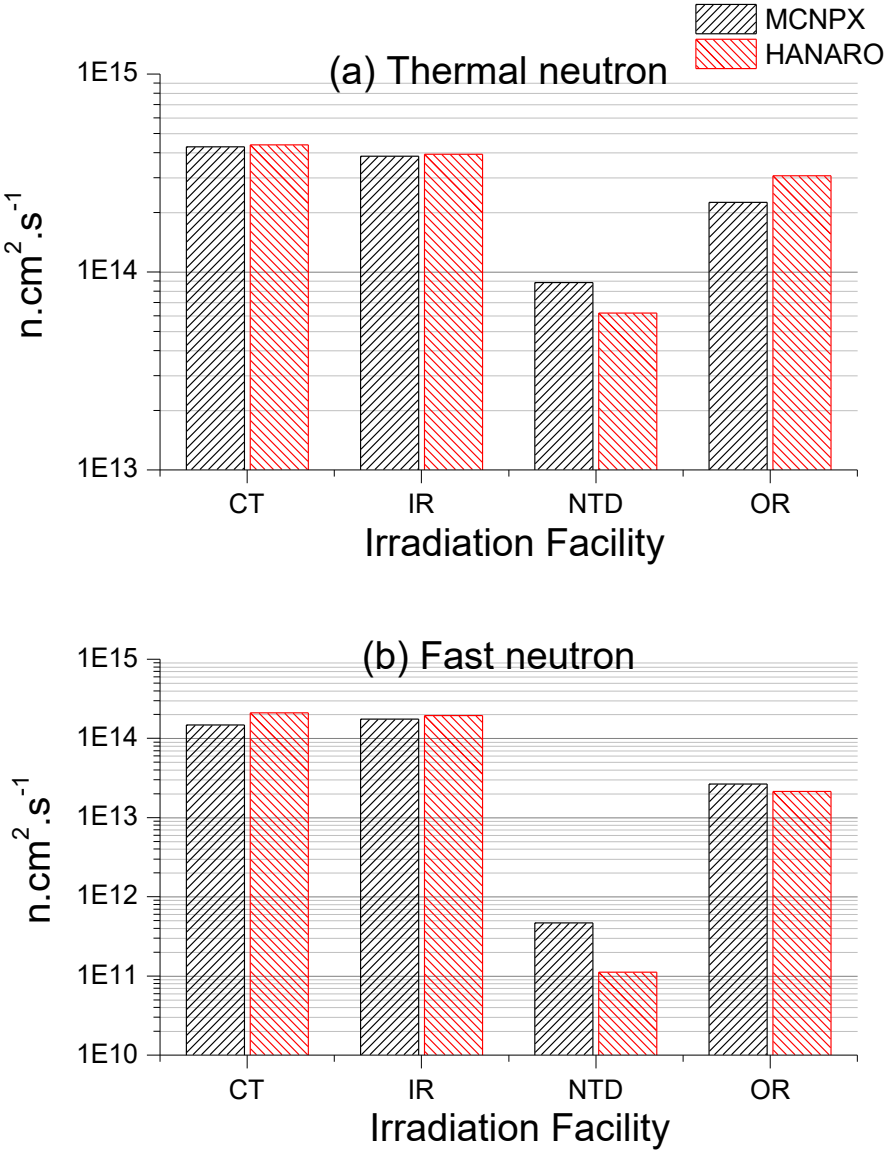

Figure 4. Thermal (a) and fast (b) neutron flux comparison between MCNPX and HANARO data at CT, IR, NTD, and OR.

Figure 5 presents the neutron flux spectra at three representative irradiation sites of the reactor core. All spectra exhibit the characteristic thermal peak around 10^{-8}–10^{-7} MeV, consistent with a Maxwellian distribution typical of light water moderated systems. The CT achieves the highest thermal neutron flux, exceeding 10^{13} n/cm²·s·MeV, followed closely by the OR, while the NTD remains distinctly lower, reflecting the intentional suppression of epithermal and fast components to meet the specific requirements of silicon doping applications. In the epithermal region (10^{-6}–10^{-3} MeV), the CT maintains a slightly elevated flux compared to the OR, owing to its central position within the core, whereas the NTD shows a marked reduction. A similar trend is observed in the fast energy region (>0.1 MeV), where the CT retains the strongest flux, followed by the OR, with the NTD again strongly attenuated. These spectral differences highlight the functional specialization of each facility: the CT provides the highest flux levels suitable for demanding fuel and materials testing, the OR serves as a flexible site for general irradiation purposes, and the NTD offers a moderated environment optimized for semiconductor applications. The overall spectral shapes and relative magnitudes are consistent with reported measurements and simulations of HANARO.

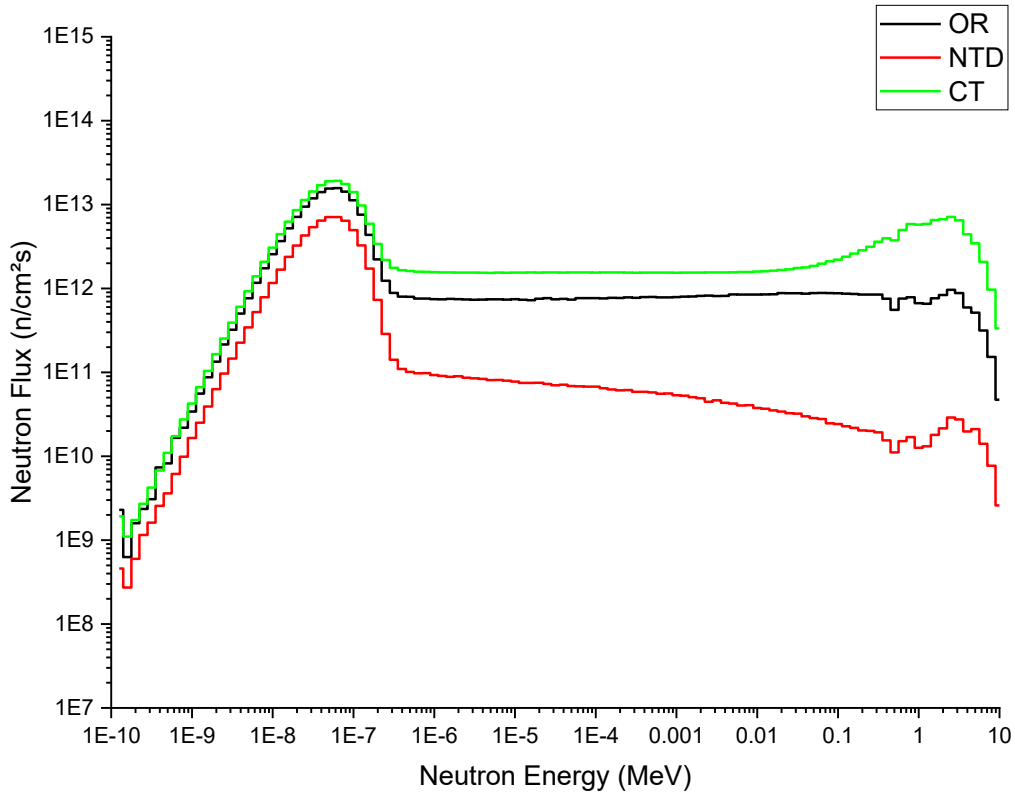

Figure 5. Neutron flux spectra at the CT, OR, and NTD facilities.

Having successfully validated the MCNPX model against experimental benchmarks for k_{eff}, burnup, and flux values, the model was then applied to generate a detailed neutron flux map of the core model. Figure 6 illustrates the MCNPX-calculated neutron flux distributions in the MCNPX core model, showing the core configuration (a) and the fast (b) and thermal (c) flux profiles. The top (a) panel provides a schematic of the reactor core, depicting the central active fuel region (hexagonal configuration) encased by the heavy water reflector and the outer pool, while marking key irradiation sites such as NTD positions, OR channels, and central channels (CT, IR1, IR2). The middle panel (b) illustrates the fast neutron flux distribution, showing maximum intensity within the central fuel assemblies. This is consistent with theoretical

expectations, as fast neutrons are produced directly by fission events, and their flux naturally diminishes with increasing distance from the fission sites. The spatial localization of high fast-neutron flux directly informs irradiation capabilities, identifying regions suitable for experiments or processes that require high-energy neutrons, such as displacement damage studies or fast-neutron activation (Marsden & Hall, 2012). In contrast, the right panel (c) depicts the thermal neutron flux, which peaks not within the fuel itself but in the surrounding heavy water reflector. This behavior arises from the moderation process: fast neutrons escaping the core are effectively slowed, or "thermalized," by collisions with hydrogen nuclei in the heavy water, creating a spatial region of enhanced thermal flux (Tsuruta, 2002)

Such thermal flux peaks are crucial for irradiation applications requiring high thermal neutron exposure, including isotope production, neutron activation analysis (NAA), and silicon doping. Collectively, the figure confirms the expected inverse spatial distributions of fast and thermal neutrons—fast neutron flux concentrated in the core and thermal flux enhanced in the reflector—while directly linking these distributions to the reactor's practical irradiation capabilities across multiple experimental and industrial applications. Thermal and fast neutron flux maps further define irradiation and beamline conditions, informing applications such as neutron radiography, NAA, and boron neutron capture therapy (BNCT). Flux data also guide beam port design to maximize thermal neutron flux while minimizing fast-neutron and gamma contamination.

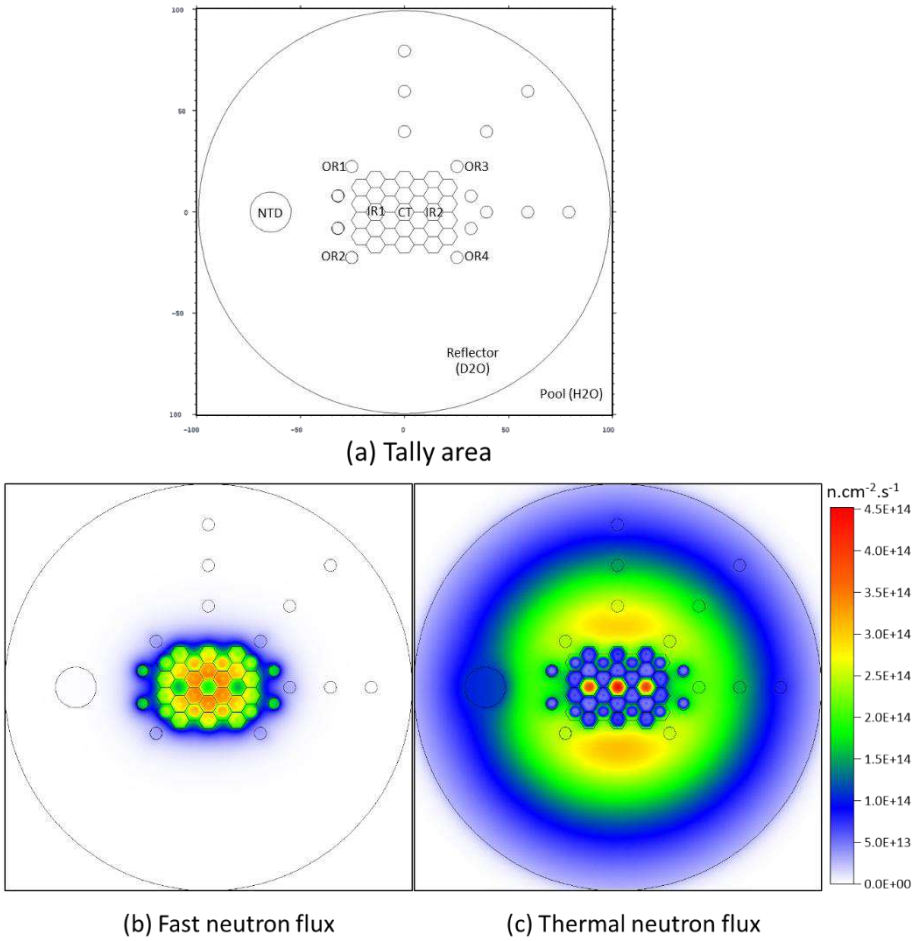

Figure 6. MCNPX-calculated neutron flux distributions.

Power distribution

The neutron flux distribution directly dictates the power distribution since local power density depends on the fission rate, which is governed by the flux. Figure 7 presents the simulated power density distribution across the core, generated using MCNPX. The distribution shows the expected profile, with maximum power concentrated at the central region and decreasing towards the periphery, consistent with the neutron flux profile and diffusion theory predictions (Lamarsh & Baratta, 2001). Within individual hexagonal assemblies, a clear "power peaking" effect is observed, where fuel rods along the outer edges exhibit higher power densities than those at the center. This intra-assembly peaking arises because thermalized neutrons from the water moderator between assemblies preferentially enhance fission at the fuel–moderator boundary, a well-established effect in lattice physics. Both the core-wide and intra-assembly patterns are consistent with reactor physics theory and previous validated neutronic analyses of HANARO and similar research reactors.

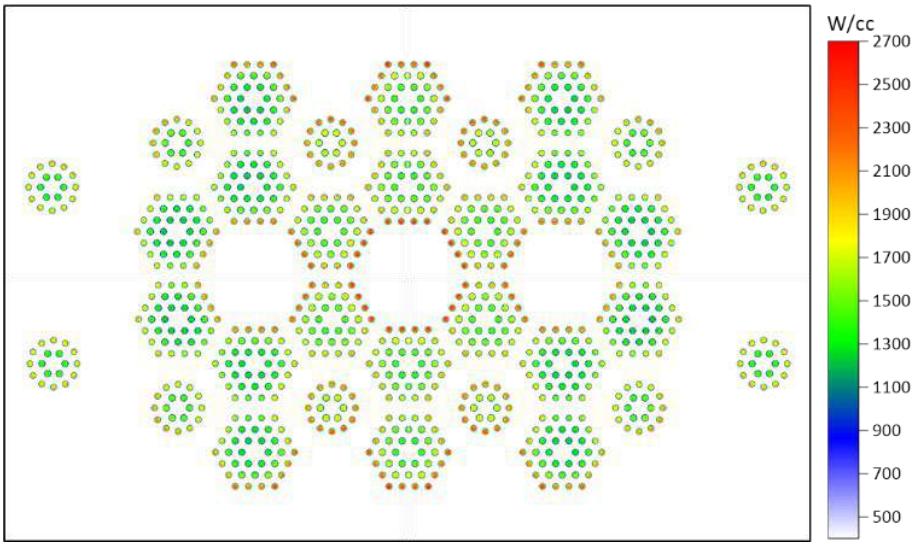

Figure 7. MCNPX-calculated power density distributions.

Figure 8 presents the analysis of power peaking factors for selected fuel assemblies (FAs) in the MCNPX core model. The top panel (a) illustrates a quarter-core symmetry model, a standard approach in neutronic simulations that reduces computational demand while maintaining fidelity. Within this model, nine fuel assemblies (FA1–FA9) are represented, with fuel rods and the surrounding heavy water reflector in blue. Additional core features, such as an empty channel and a light water region, are also included. The arrangement of fuel assemblies, whether centrally located or positioned near the periphery, strongly influences neutron flux distribution and local power generation (Lamarsh & Baratta, 2001). The right bottom plots the power peaking factor of each assembly as a function of operational time. The power peaking factor, defined as the ratio of the maximum power density in a given assembly to the average power density across the core, provides a measure of relative power contribution. Assemblies positioned near the reflector (FA2, FA3, FA5, and FA8) exhibit factors greater than unity, as neutron reflection enhances their local flux and power output. In contrast, centrally located assemblies (FA1 and FA7) remain close to or slightly below unity, consistent with the more uniform neutron flux in the core interior. FA6 and FA9 exhibit power peaking factors below 1.0 despite being adjacent to the heavy water reflector. This behavior can be attributed to their comparatively greater distance from the core center, which reduces the

overall neutron flux available to these positions relative to other peripheral fuel assemblies. FA4 shows the lowest factor, remaining below 0.9, due to its placement near a region with reduced thermal neutron flux.

In summary, the maximum assembly-wise power peaking factors are observed in peripheral assemblies FA2, FA3, FA5, and FA8, remaining below 1.1, while the highest pin-wise peaking occurs along the fuel–moderator boundaries within these assemblies. Central assemblies (FA1 and FA7) and other peripheral assemblies (FA6, FA9) show factors at or below unity, reflecting a uniform and well-controlled power distribution. These results indicate that all fuel rods operate within safe thermal margins, with no risk of localized overheating, supporting the overall safety and reliable performance of the core.

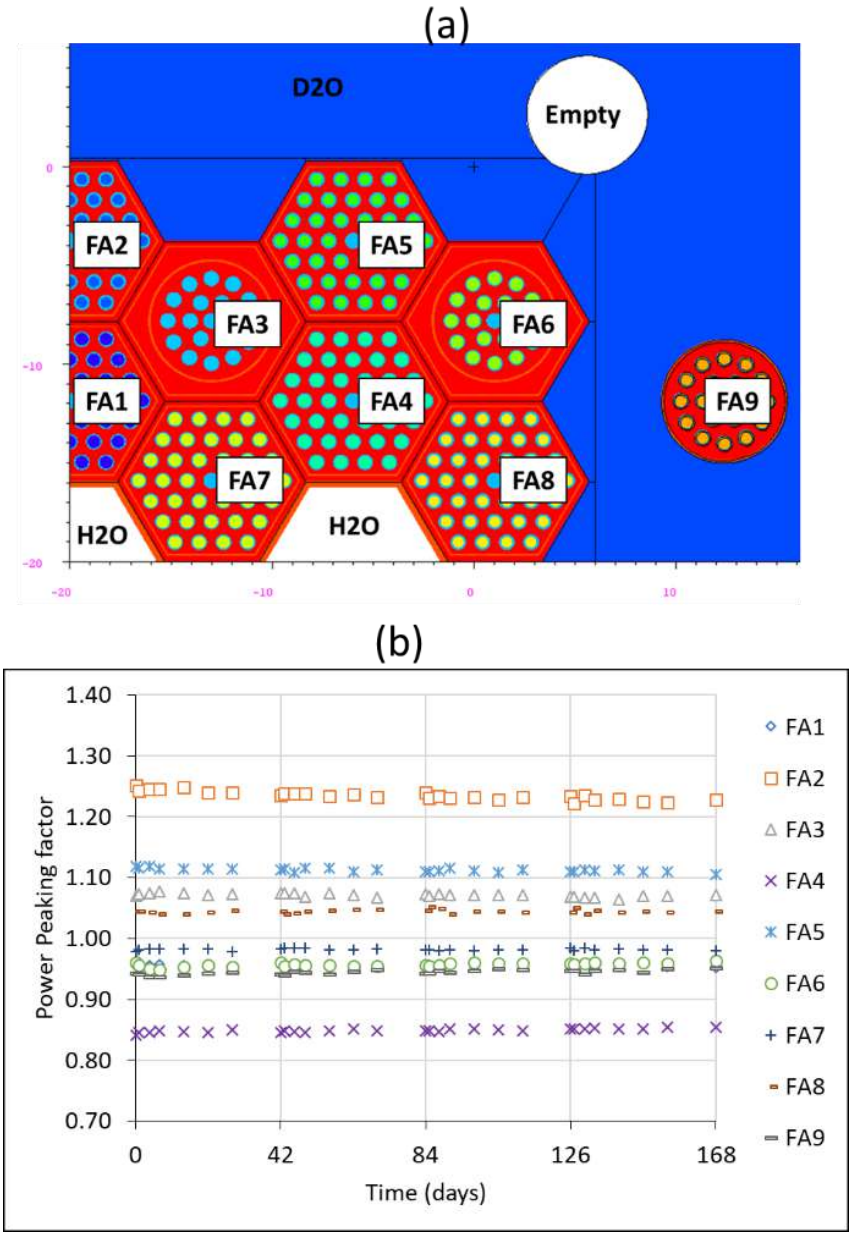

Figure 8. MCNPX-calculated power peaking factor.

PRELIMINARY CORE DESIGN CONSIDERATIONS FOR THE MALAYSIAN MPR

Based on the current, limited analysis and following the successful validation of the MCNPX model against the HANARO reference reactor, this section tentatively outlines a preliminary core design and operational concept for the proposed Malaysian MPR. This initial concept attempts to leverage the validated model to ensure the reactor could potentially fulfill national objectives in research, isotope production, and neutron beam aplication.

Core Design and Operational Concept

For this initial conceptualization, the Malaysian MPR might adopt a hybrid configuration, drawing a parallel to HANARO, by combining 36-rod hexagonal and 18-rod cylindrical fuel assemblies. The core is envisioned to consist of 32 assemblies utilizing low-enriched uranium silicide dispersion fuel, clad in aluminum, with an enrichment of 19.75%. A heavy water reflector is proposed to potentially enhance neutron economy and increase thermal flux in the irradiation channels. Preliminary simulations suggest a central thermal neutron flux of approximately 4.3×10^{14} $n\cdot cm^{-2}\cdot s^{-1}$, a level which should be sufficient for a broad range of high-flux neutron applications.

Fuel management is currently based on a batch refueling scheme, with 28-day operating cycles followed by 14-day shutdowns for maintenance and shuffling. The model estimates a fuel residence time of about 175 full-power days, corresponding to an average burnup potentially exceeding 50% of the initial U-235. This design is intended to ensure efficient fuel utilization, compliance with international LEU standards, and operational flexibility. The calculated k_{eff} values appear to confirm that the fresh core could offer adequate excess reactivity to remain supercritical over each cycle, even when accounting for xenon transients.

Based on HANARO's operational practices, a proposed refueling scheme would adopt a frequent, partial core replacement strategy (Rho, 1997; Lee et al, 2009). This method is designed to maintain a consistent, high neutron flux necessary for continuous research and isotope production. The reactor would tentatively operate on a short, fixed 28-day cycle of full-power operation, followed by a scheduled 14-day outage for maintenance and fuel handling, resulting in a refueling opportunity approximately every six weeks. During each of these planned outages, only a small batch of the most depleted fuel assemblies would be discharged. The remaining partially-spent assemblies would be strategically shuffled to new, optimized core locations to maximize their energy use and flatten the power distribution. Finally, a new batch of fresh fuel would be loaded into the vacant positions.

Spent Fuel Management Considerations

As a point of reference, HANARO operates on a partial core refueling scheme, typically replacing 7–8 fuel assemblies per year. Annual refueling removes only a fraction of the core at a time to maintain core reactivity and ensure stable power operation. This gradual replacement strategy is shown to support effective burnup management and preserves safety margins, with discharged fuel remaining in the wet storage pool pending further management or disposal Lee et al, 2009). Each standard fuel assembly is known to contain approximately 3.0–3.2 kg of uranium, with 19.75% enrichment in U-235. Based on the average annual replacement of 7–8 assemblies, approximately 23–25 kg of total uranium is discharged per year, comprising

~4.65 kg of U-235 and ~18.6 kg of U-238. Assuming continuous operation for a typical research reactor lifespan of 50 years, a total of approximately 375 fuel assemblies would be discharged, implying that the wet storage pool must have sufficient capacity to store at least this number of assemblies safely, accounting for decay heat removal and radiation shielding. These data provide a quantitative basis for estimating the annual fuel inventory, burnup management, and core fuel strategy, and serve as a valuable reference for designing spent fuel handling practices in similar research reactors.

Over a 50-year lifespan, HANARO's partial core refueling of 7–8 assemblies per year would discharge approximately 375 assemblies, totaling about 1,163 kg of uranium, including 230 kg of U-235. With an effective burnup of roughly 30% per assembly, around 69 kg of U-235 would be consumed, allowing gradual fuel utilization while maintaining core reactivity and safety margins. The wet storage pool must accommodate all discharged assemblies, ensuring adequate decay heat removal and radiation shielding.

Preliminary Utilization Planning

The proposed Malaysian MPR could potentially host a range of irradiation facilities to meet anticipated research and industrial demands. Approximately six in-core irradiation sites are envisioned to be placed within the active core and reflector to support high-flux applications such as neutron transmutation doping of silicon and radioisotope production. For conventional silicon, HANARO's NTD thermal flux of 8.83×10^{13} n·cm^{-2}·s^{-1} is sufficient to produce high-quality semiconductor-grade material. For emerging semiconductors like silicon carbide (SiC), which rely on fast neutron transmutation, the required fluence is typically 10^{18}–10^{19} n·cm^{-2}. At the NTD facility, the fast flux is only ~10^{11} n·cm^{-2}·s^{-1}, making it impractical for SiC doping, whereas in the central trap, where fast flux reaches ~10^{14} n·cm^{-2}·s^{-1}, the required fluence could be achieved in roughly 1–2 days of continuous irradiation, demonstrating that high-flux regions are essential for producing doped SiC efficiently while HANARO's NTD thermal flux remains suitable for conventional silicon. Similarly, the central trap and inner reflector regions, with fluxes potentially exceeding 10^{14} n·cm^{-2}·s^{-1}, would enable efficient production of medical isotopes such as molybdenum-99 (Mo-99), the precursor of technetium-99m (Tc-99m). In addition, 15 out-of-core irradiation sites are planned around the reflector and pool, operating at lower fluxes to support activities such as neutron activation analysis and materials testing under controlled neutron exposure. For comparison, HANARO's substantial in-core capacity, comprising seven irradiation holes (three hexagonal and four circular), complemented by over ten reflector positions and specialized facilities including beam tubes and NTD sites (Choo et al., 2014; Lee, Ahn & Lim, 2007).

CONCLUSIONS

The preliminary neutronic design and analysis for the Malaysian Multi-Purpose Research Reactor, benchmarked against the 30 MWth South Korean HANARO reactor, has successfully achieved all its stated objectives and established a robust technical foundation for the project. The study confirmed the suitability of the methodology and reference design. A detailed MCNPX model of the HANARO reactor was successfully developed and validated against experimental data for key parameters such as effective multiplication factor, burnup, and neutron flux values at various irradiation sites. The model demonstrated strong agreement, confirming its accuracy and reliability as a predictive tool. The validated model was then used

to propose a preliminary core design and fuel management strategy for the Malaysian MPR. This included defining the hybrid fuel configuration, predicting a core residence time of 175 full-power days, and analyzing the core's operational behavior and power distribution. The insights gained from this analysis, particularly regarding the effects of the heavy water reflector and power peaking, are essential for optimizing fuel management and ensuring the reactor meets its safety and performance goals.

ACKNOWLEDGEMENT

The authors would like to express their sincere gratitude to the Malaysian Nuclear Agency, specifically the Technical Support Division under the Reactor Technology Centre, for providing all the necessary resources and support to conduct this study. Their invaluable assistance was instrumental in the successful completion of this research.

CREDIT AUTHORSHIP CONTRIBUTION STATEMENT

Mohamad Hairie Rabir: Writing – original draft. Norfarizan Mohd Said: Writing – review & editing. Mark Dennis Usang: Writing – review & editing. Abi Muttaqin Jalal Bayar: Writing – review & editing. Na'im Syauqi Hamzah: Writing – review & editing. Phongsakorn Prak Tom: Writing – review & editing. Hasniyati Md Razi: Writing – review & editing. Muhammad Khairul Ariff Mustafa: Writing – review & editing. Julia Abdul Karim: Writing – review & editing.

DECLARATION OF COMPETING INTEREST

The authors declare that they have no known competing financial interests or personal relationships that could have appeared to influence the work reported in this paper.

REFERENCES

ANSTO. (n.d.). *Neutron activation analysis and neutron irradiation*. OPAL Multi-Purpose Reactor. Retrieved September 25, 2025, from https://ansto.com/facilities/opal-multi-purpose-reactor/neutron-activation-analysis-and-neutron-irradiation

Chae, H., et al. (1996). Design characteristics and startup tests of HANARO. *Journal of Nuclear Science and Technology*, *33*(7), 527–535. https://doi.org/10.1080/18811248.1996.9733541

Chae, H., Lee, C. S., Park, J. M., Kim, H., & Kim, Y. S. (2018). Performance of U3Si–Al dispersion fuel at HANARO full-power condition. *Nuclear Engineering and Technology*, *50*(6), 899–906. https://doi.org/10.1016/j.net.2018.05.004

Choo, K. N., Cho, M. S., Yang, S. W., & Park, S. J. (2014). Contribution of HANARO irradiation technologies to national nuclear R&D. *Nuclear Engineering and Technology*, *46*(4), 501–512. https://doi.org/10.5516/NET.07.2014.006

Goorley, J. E. B. V., James, M. R., Booth, T. E., Brown, F. B., Bull, J. S., Cox, L. J., Durkee, J. W., Elson, J. S., Fensin, M. L., Forster, R. A., Hendricks, J. S., Hughes, H. G., Johns, R. C., Kiedrowski, B. C., Martz, R. L., Mashnik, S. G., McKinney, G. W., Pelowitz, D. B., Prael, R. E., ... Werbein, S. (2011). *MCNP6: The next generation Monte Carlo transport code* (Report No. LA-UR-11-05078). Los Alamos National Laboratory.

Kim, J., Lee, B. C., Chae, H., & Park, J. M. (2016). Neutron flux characterization of irradiation holes for irradiation test at HANARO. *EPJ Web of Conferences*, *106*, 01004. https://doi.org/10.1051/epjconf/201610601004

Lamarsh, J. R., & Baratta, A. J. (2001). *Introduction to nuclear engineering* (3rd ed.). Prentice Hall.

Lee, C. S., Ahn, G. H., & Lim, I. C. (2008). Utilization of the irradiation holes in HANARO. In *Proceedings of the IAEA Conference on Research Reactor Utilization, Safety, Decommissioning, Fuel and Waste Management (ICRR 2007)* (p. 5). IAEA. https://www.pub.iaea.org/MTCD/publications/PDF/P1360_ICRR_2007_CD/Papers/C.S.%20Lee.pdf

Lee, M., Lee, K., Park, S., & Choi, K. (2009). *Current status of the spent fuel management in HANARO* [Conference presentation]. 12th International Group on Research Reactors (IGORR) Conference.https://www.igorr.com/_media/proceedings:2009_igorr12:mun_lee.pdf

Los Alamos National Laboratory. (2011). *MCNPX user's manual version 2.7.0*. Los Alamos, NM, USA.

Marsden, B. J., & Hall, G. N. (2012). Graphite in gas-cooled reactors. In *Comprehensive Nuclear Materials* (Vol. 4, pp. 325–390). Elsevier. https://doi.org/10.1016/B978-0-08-056033-5.00092-6

Ministry of Science, Technology and Innovation Malaysia (MOSTI). (2023). *Dasar Teknologi Nuklear Negara (DTNN) 2030*. https://www.mosti.gov.my/en/dasar-teknologi-nuklear-negara-dtnn-2030/

Rho, K. H. (1997, March). *In-core fuel management practice in HANARO* [Conference presentation]. International Topical Meeting on Research Reactor Fuel Management (RRFM '97), Delft, Netherlands. https://inis.iaea.org/records/ps1bm-x3t90

Shin, J. (2023). *Current status of HANARO operation and challenging issues*. Korea Atomic Energy Research Institute (KAERI). https://www.trtr.org/wp-content/uploads/2023/05/Current-Status-of-HANARO-Operation-and-Challenging-Issues-Jinwon-Shin.pdf

Tsuruta, H. (2002). *Neutronics design of upgraded JRR-3 research reactor*. OECD Nuclear Energy Agency. https://www.oecd-nea.org/upload/docs/application/pdf/2020-07/neacrp-a-1984-0653.pdf

Jurnal Sains Nuklear Malaysia, 2025, 37(No. 2): 20 – 33
ISSN: 2232-0946

VALIDATION OF A RADIOCHEMICAL SEPARATION AND ALPHA SPECTROMETRIC METHOD FOR DETERMINATION OF ^{234}U, ^{235}U, AND ^{238}U IN ENVIRONMENTAL SAMPLES

Nurrul Assyikeen Md. Jaffary*, Jalal Sharib @ Sarip, Chriscius Anthonius and Mohd Tarmizi Ishak

Environment & Waste Technology Division
Malaysian Nuclear Agency
Bangi, 43000 Kajang, Malaysia
*Corresponding author: assyikeen@nm.gov.my

ABSTRACT

This study presents the validation of a radiochemical separation and alpha spectrometric method for the determination of uranium isotopes (^{234}U, ^{235}U, and ^{238}U) in environmental samples. The procedure was evaluated using two International Atomic Energy Agency (IAEA) certified reference materials (CRMs), namely IAEA-385 (Irish Sea Sediment) and IAEA-384 (Fangataufa Sediment), to assess its analytical performance. Validation parameters included selectivity, accuracy, precision, repeatability, ruggedness, and robustness. The calculated u-scores and z-scores were within acceptable limits, and relative bias values demonstrated good agreement with certified values. Inter-analyst comparison using IAEA-385 confirmed the method's ruggedness, while consistent performance across different CRMs demonstrated its robustness. The validated procedure provides a reliable and standardized approach for uranium isotope analysis in environmental matrices and is established at the Radiochemistry and Environment Laboratory, Malaysian Nuclear Agency, for routine environmental monitoring applications.

Keywords: uranium isotope, alpha spectrometry, method validation, radiochemistry

ABSTRAK

Kajian ini membentangkan penentusahan kaedah pemisahan radiokimia dan pengukuran menggunakan spektrometri alfa bagi penentuan isotop uranium (^{234}U, ^{235}U dan ^{238}U) dalam sampel alam sekitar. Prosedur ini dinilai menggunakan dua bahan rujukan diperakui (CRM) daripada Agensi Tenaga Atom Antarabangsa (IAEA), iaitu IAEA-385 (Sedimen Laut Ireland) dan IAEA-384 (Sedimen Fangataufa), bagi menilai prestasi analitik kaedah tersebut. Parameter penentusahan yang dinilai merangkumi ketertentuan, ketepatan, kejituan, kebolehulangan, kekasaran dan keteguhan. Nilai u-score dan z-score yang diperoleh adalah dalam julat penerimaan, manakala bias relatif menunjukkan persetujuan yang baik dengan nilai diperakui. Perbandingan antara penganalisis menggunakan IAEA-385 mengesahkan kekasapan kaedah, manakala prestasi yang konsisten merentasi CRM yang berbeza membuktikan keteguhannya. Prosedur yang telah ditentusahkan ini menyediakan pendekatan yang boleh dipercayai dan piawai bagi analisis isotop uranium dalam matriks alam sekitar serta telah dilaksanakan di Makmal Radiokimia dan Alam Sekitar, Agensi Nuklear Malaysia, untuk aplikasi pemantauan alam sekitar secara rutin.

Kata kunci: *isotop uranium, spektrometri alfa, penentusahan kaedah, radiokimia*

INTRODUCTION

Accurate analysis of uranium in sediment samples is crucial for environmental monitoring, pollution assessment, and regulatory compliance (IAEA 1997). Uranium, a naturally occurring radioactive element, poses significant health and ecological risks at elevated concentrations (IAEA 2005). Accurate quantification and monitoring of uranium levels in environmental samples are essential for managing these risks (EPA 2006). This study presents the validation of the developed uranium analysis procedure using radiochemical separation and alpha spectrometry, conducted at the Radiochemistry and Environment Group, Malaysian Nuclear Agency.

Method validation is critical in analytical chemistry to ensure the reliability and accuracy of analytical methods (Rambla-Alegre et al. 2012). Key parameters evaluated during validation include selectivity, accuracy, precision, repeatability, and robustness. Selectivity ensures the method accurately identifies the target analyte in the presence of other substances. Accuracy measures how closely the results agree with the true value (Magnusson & Örnemark 2014). Precision assesses the repeatability or reproducibility of results under consistent conditions.

Repeatability examines the consistency of results under the same conditions, while ruggedness tests the method's reliability across variations such as different operators or equipment settings. Robustness evaluates the method's reliability when deliberately introducing minor variations in experimental conditions. Linearity demonstrates how well the method generates results that are directly proportional to the analyte's concentration. Limits of detection (LOD) and quantitation (LOQ) are crucial, with LOD being the lowest detectable concentration and LOQ the lowest concentration that can be quantitatively determined with acceptable accuracy and precision.

This study aims to evaluate key aspects of analytical methods to ensure their reliability and accuracy. The focus is on accuracy, precision, repeatability, specificity, and specific aspects of robustness and ruggedness. Other important factors are still being investigated and will be discussed in future study. This ongoing research aims to enhance the analytical capability of the laboratory, ensure the generation of reliable and traceable results, and strengthen laboratory quality management practices in alignment with ISO/IEC 17025 principles.

METHODOLOGY

Reagents and Materials

All reagents were of analytical grade. Concentrated nitric acid (HNO_3, 65%), hydrochloric acid (HCl, 37%), hydrofluoric acid (HF, 40%), perchloric acid ($HClO_4$, 70%), sulfuric acid (H_2SO_4, 95%), hydrogen peroxide (H_2O_2, 30%), and ammonium hydroxide (NH_4OH, 28%) were used for digestion and chemical separation. Diluted acid solutions of defined molarity were prepared from the concentrated stock solutions using distilled water for subsequent ion-exchange and extraction chromatography steps. A NIST-traceable ^{232}U solution was employed as a tracer to monitor chemical recovery throughout the procedure. Anion exchange resin AG 1-X2 (chloride form, 100–200 mesh) and TRU-Spec extraction chromatography resin were used for uranium separation and purification. Polished stainless steel discs were used for electrodeposition prior to alpha

spectrometric measurement. Certified reference materials IAEA-385 and IAEA-384 were used for performance evaluation.

Radiochemical Separation and Source Preparation

Approximately 0.5 g of sediment CRM was accurately weighed into a 250 mL Teflon beaker and moistened with a small volume of dilute nitric acid (~1–2 M HNO_3) to form a homogeneous slurry. Approximately 0.5 Bq of ^{232}U tracer was then added prior to digestion to monitor chemical recovery and assess the efficiency of the separation procedure. The sample was digested using a mixed-acid consisting of hydrofluoric acid, nitric acid, perchloric acid, and hydrogen peroxide. The beaker was heated on a controlled hot plate until dryness to ensure complete dissolution of silicate and refractory components. Repeated evaporation with concentrated nitric acid was performed to eliminate residual fluoride complexes and convert uranium into a nitrate medium suitable for anion exchange separation. Mixed-acid digestion using $HF–HNO_3–HClO_4$ is widely applied for the decomposition of environmental matrices containing silicate minerals (IAEA 1997).

The dried residue was dissolved in 8 M nitric acid and loaded onto a pre-conditioned AG 1-X2 anion exchange column. In concentrated nitric acid medium, uranium forms stable anionic nitrate complexes (e.g., $UO_2(NO_3)_3^-$) that are selectively retained on the resin, while most matrix elements pass through. The column was washed with additional 8 M nitric acid to remove residual matrix constituents. The uranium fraction was subsequently eluted and evaporated to dryness. Anion exchange in strong nitric acid medium is a well-established method for uranium separation from complex environmental matrices, as described by Horwitz et al. (1992, 1993) and further applied in environmental uranium determination by Jia et al. (2002).

For further purification, the residue was dissolved in 2 M nitric acid and loaded onto a TRU-Spec extraction chromatography column that had been preconditioned with distilled water followed by 2 M nitric acid. The column was sequentially washed with nitric acid solutions of decreasing molarity to remove interfering actinides and residual matrix components. Uranium was eluted using ammonium bioxalate solution, and the eluate was evaporated to dryness. TRU-Spec resin provides enhanced selectivity for actinides and improves alpha spectral quality by minimizing co-eluting species (Horwitz et al. 1993; Jia et al. 2002)

The purified uranium fraction was subjected to electrodeposition to produce a thin, uniform source suitable for alpha spectrometry. The residue was treated with perchloric and sulfuric acids to convert the uranium into a sulfate medium, followed by controlled evaporation. The final solution was adjusted to pH 2.0–2.2 using dilute sulfuric acid, and a small amount of sodium dodecyl sulfate was added to improve deposition quality. The solution was transferred to an electrodeposition cell fitted with a polished stainless steel disc. Electrodeposition was carried out for one hour under controlled current conditions to obtain a thin and homogeneous uranium layer. After deposition, the disc was rinsed, dried, and briefly flamed to ensure adherence of the deposit. Electrodeposition is widely employed in alpha spectrometric analysis to minimize self-absorption and achieve optimal peak resolution (Gaburo et al. 2006).

Alpha Spectrometric Measurement

The prepared discs were measured using an ORTEC Octete Plus alpha spectrometer equipped with silicon surface barrier detectors. Energy calibration was performed using multi-alpha reference standards prior to sample analysis. Counting times were selected to achieve adequate statistical precision, particularly for the low-abundance isotope ^{235}U.

Activity concentrations were calculated using a tracer-based isotope dilution approach. The activity of each uranium isotope was determined from the ratio of net analyte count rate to net tracer count rate, multiplied by the certified activity of the ^{232}U tracer and normalized to sample mass, as expressed in Eq. 1. Blank corrections were applied to both analyte and tracer count rates, and decay correction factors were incorporated to account for time differences between reference, separation, and measurement dates. This approach inherently corrects for chemical recovery and counting efficiency variations.

$$A_A = \frac{A_{tracer} \cdot W_t \frac{(R_{S1} - R_{B1})}{(R_{S2} - R_{B2})}}{W_s} \cdot f_1 \cdot f_2 \ldots \text{Eq. 1}$$

Where:

A_A = activity concentration of analyte
A_{tracer}= certified activity concentration of tracer at reference date
W_t = mass of tracer added (kg)
W_s = mass of sample (kg)
R_{S1} = gross count rate of analyte (counts s^{-1})
R_{B1}= blank count rate of analyte (counts s^{-1})
R_{S2} = gross count rate of tracer (counts s^{-1})
R_{B2}= blank count rate of tracer (counts s^{-1})
f_1 = decay correction factor for tracer
f_2 = decay correction factor for analyte

Method Performance Evaluation and Validation Criteria

Selectivity was determined by evaluating the energy spectrum produced, ensuring the method could accurately identify uranium isotopes in the presence of other components (NATA 2006). Accuracy was assessed by comparing measured values to known CRM values, calculated using the u-score using Eq. 2 below:

$$U - score = \frac{|x_{lab} - x_{ref}|}{\sqrt{Unc_{ref}^2 + Unc_{lab}^2}} \ldots \text{Eq. 2}$$

Where X_{lab} is the mean value from measurement; X_{ref} is the reference value, Unc_{ref} is the standard deviation of the reference value, and Unc_{lab} is the standard deviation of the analytical value. In addition to the u-score, the z-score was calculated for accuracy evaluation, defined by Eq. 3 below:

$$Z - score = \frac{|X_{lab} - X_{ref}|}{Std} \text{ ...Eq. 3}$$

Where X_{ref} is the expected activity, and std is the standard deviation. The z-score measures how many standard deviations an observed value is from the expected value, providing a standardized way to compare results.

For interpretation, the u-score was evaluated using critical values based on statistical significance. A u-score < 1.64 indicates that the results do not differ significantly, 1.64 ≤ u-score < 2.58 suggests that the results may not differ significantly, and u-score ≥ 2.58 indicates that the results are probably significantly different. For the z-score, interpretation follows commonly applied proficiency testing thresholds (Thompson et al. 2006; ISO 13528:2015), where $|z| \leq 2$ is satisfactory, $2 < |z| < 3$ is questionable, and $|z| \geq 3$ is unsatisfactory.

Relative bias, b (%) was also calculated to measure deviation from true values, using Eq.4 below (Eurachem 1998; Guérin & Dai 2015):

$$b(\%) = \frac{X_{lab} - X_{ref}}{X_{ref}} x100 \text{ ...Eq. 4}$$

The relative standard deviation (RSD) is calculated by multiplying the standard deviation of the sample set by 100% and then dividing it by the sample set average. The RSD is expressed as a percentage. Typically, the acceptance criterion for accuracy, precision, and repeatability of data is expressed in % RSD (Sushila Dagadu Chavan & Deepa Mahendra Desai 2022):

$$\%RSD = \frac{S}{\bar{x}} x100 \ldots \text{Eq. 5}$$

Repeatability was assessed by the closeness of agreement between successive measurements of the same sample under the same conditions, including the same radiochemical method, measuring instrument, and location, with measurements repeated over a short period. Ruggedness was demonstrated by obtaining consistent results from three different analysts using IAEA-385, while robustness was highlighted by the method's consistent performance across various CRMs. Additionally, the efficiency of the radiochemical separation process was confirmed by calculating the recovery of the ^{232}U tracer, comparing the measured activity to the known spiked activity, with high recovery rates indicating effective separation and reliable quantification of uranium isotopes in sediment samples. This comprehensive validation ensured the developed procedure was reliable and suitable for routine uranium analysis in sediment samples.

RESULTS AND DISCUSSION

Selectivity

Selectivity was evaluated by comparing the measured alpha peak energies with the evaluated nuclear decay data for uranium isotopes. According to the NuDat 3.0 database (National Nuclear Data Center, 2023). The principal alpha energies are 4196 keV for ^{238}U, 4678–4679 keV for ^{235}U, 4774 keV for ^{234}U, and approximately 5320 keV for the ^{232}U tracer.

The measured regions of interest (ROI) summarized in Table 1 were centered around these expected energies. The observed peak centroids fell within the detector resolution limits and showed deviations of less than ±1% relative to the theoretical energies. Such deviations are within the acceptable energy calibration tolerance for alpha spectrometry and are consistent with typical detector full width at half maximum (FWHM) performance (Knoll 2010).

Furthermore, no overlapping peaks or spectral interferences from other alpha-emitting radionuclides were detected in the spectrum (Figure 1). The energy separation between adjacent uranium peaks substantially exceeded the typical detector resolution of silicon surface barrier detectors, ensuring adequate spectral discrimination. These results confirm adequate spectral resolution and demonstrate that the developed method provides sufficient selectivity for uranium isotope determination in sediment samples.

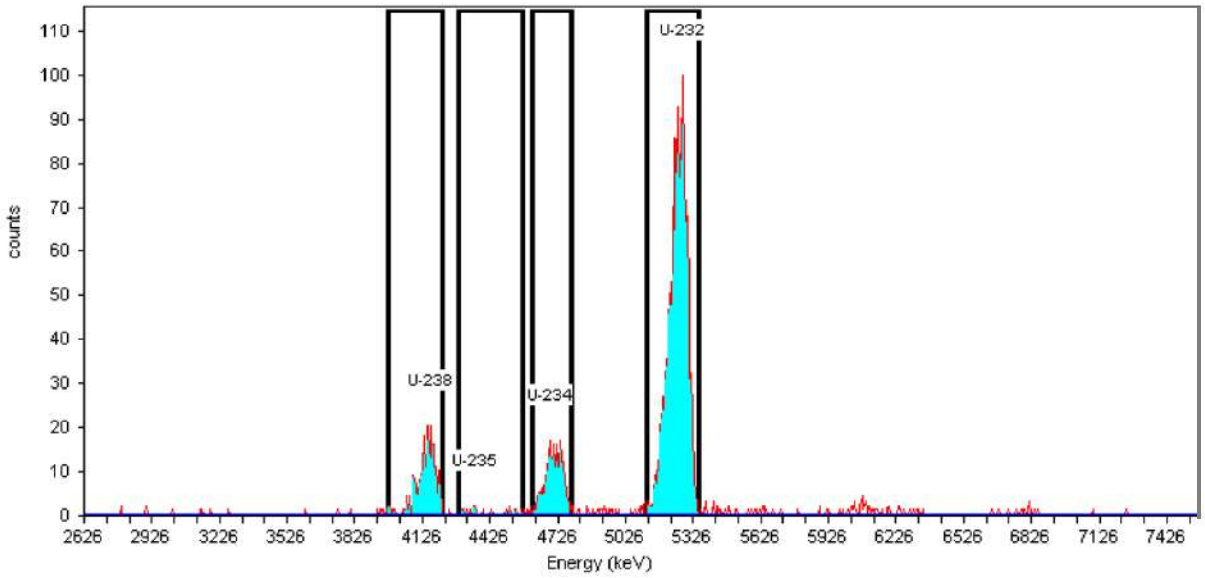

Figure 1 Uranium isotopes peak spectrum

Table 1 ^{234}U, ^{235}U, and ^{238}U energy range of interest (ROI) analysed for IAEA-385

Sample no.	^{234}U		^{235}U		^{238}U		^{232}U	
	Min keV	Max keV	Min keV	Max keV	Min keV	Max keV	Min keV	Max keV
1	4577.82	4790.66	4322.42	4498.06	4012.55	4211.21	5146.29	5343.08
2	4577.63	4795.23	4300.28	4510.36	4031.14	4214.92	5162.58	5341
3	4587.77	4790.57	4307.29	4498.06	4012.55	4211.21	5170.04	5371.7
4	4564	4790	4286.43	4416.76	4004.53	4196	5099	5370
5	4572.49	4814.57	4277.94	4495.15	4008.28	4210.46	5125.27	5344.301
6	4561.7	4770.83	4271.37	4466.79	4024.72	4185.94	5117.322	5323.98

Accuracy and Precision

The measured activity concentrations, recoveries, u-scores, z-scores, and RSD values for IAEA-385 and IAEA-384 are summarized in Table 2. These parameters were used to evaluate method accuracy, precision, and robustness.

The calculated u-scores for ^{234}U, ^{235}U, and ^{238}U in both certified reference materials were below the critical value of 1.64, indicating that the measured results did not differ significantly from the certified values. The corresponding z-scores remained within the satisfactory performance range ($|z| \leq 2$), further confirming the trueness of the method.

Relative bias values for IAEA-385 were 2.01%, 7.14%, and 0.54% for ^{234}U, ^{235}U, and ^{238}U, respectively, reflecting minimal deviation from certified values. Similar agreement was observed for IAEA-384, confirming method reliability across different environmental matrices.

Table 2 Measurement data, u-score, z-score, and recovery for ^{234}U, ^{235}U, and ^{238}U in IAEA-385 and IAEA-384

IAEA-385 Certified value	**^{234}U (27.2±1.2 Bq/kg)**	**^{235}U (1.36±0.11 Bq/kg)**	**^{238}U (29.4±1.2 Bq/kg)**	**Recovery**
Sample no.	**Lab value (Bq/kg)**	**Lab value (Bq/kg)**	**Lab value (Bq/kg)**	
1	28.96±4.4	2.57±1.2	29.27±4.4	93.07
2	24.64±3.85	2.62±1.17	25.02±3.85	95.65
3	26.8±4.43	2.01±1.2	32.9±5.07	82.2
4	30.8±4.74	2.55±1.25	33.54±5	85.75
5	28.49±4.49	2.66±1.27	29.1±4.51	92.23
6	26.72±4.4	1.13±1.03	30.41±4.76	81.93
Mean	27.75±3.75	1.26±1.25	29.24±3.90	88.47
U-score	0.14	0.08	0.04	
Relative bias, %	2.01	7.14	0.54	
RSD, %	7.72	47.63	10.51	
Z-Score	0.25	0.16	0.05	
IAEA 384 Certified value	**^{234}U (40.3±2.2 Bq/kg)**	**^{235}U (1.76±0.12 Bq/kg)**	**^{238}U (36.4±1.2 Bq/kg)**	**Recovery**
Sample no.	**Lab value (Bq/kg)**	**Lab value (Bq/kg)**	**Lab value (Bq/kg)**	
1	35.34±4.71	3.03±1.19	42.61±5.38	96.79
2	40.51±5.00	2.95±1.12	33.95±4.35	110.02
3	39.16±5.50	2.80±1.32	36.24±5.15	78.27
4	38.11±4.63	2.82±1.05	32.97±4.13	110.82
5	35.86±4.65	1.61±0.94	31.56±4.20	103.97
Mean	37.80±4.90	2.64±1.12	35.47±4.64	
U-score	0.38	0.78	0.72	
Relative bias, %	6.21	50.11	10.40	
RSD, %	5.78	22.13	12.24	
Z-Score	1.15	1.51	0.22	

Precision

The RSD values further support the method's precision. For ^{234}U and ^{238}U, the RSD values were 7.72% and 10.51% for IAEA-385, and 5.78% and 12.24% for IAEA-384, respectively, demonstrating acceptable repeatability under the same analytical conditions. RSD values below 20% are generally considered acceptable for radiochemical methods at environmental activity levels, particularly where counting statistics influence measurement uncertainty (Magnusson & Örnemark 2014). In contrast, the higher RSD observed for ^{235}U (47.63% in IAEA-385 and 22.13% in IAEA-384) is attributable to its lower activity concentration and reduced counting statistics, which increase relative variability in alpha spectrometric measurements, and this behaviour is consistent with Poisson counting statistics rather than systematic analytical bias.

Recovery

The recovery values for ^{234}U, ^{235}U, and ^{238}U obtained for IAEA-385 and IAEA-384 are presented in Table 2 and were used to evaluate the efficiency of the radiochemical separation. For IAEA-385, individual recoveries ranged from 81.93% to 95.65%, with a mean value of 88.47%. For IAEA-384, recoveries ranged from 78.27% to 110.82%, yielding a mean of 99.98%.

In alpha spectrometric radiochemical analysis of environmental samples, recoveries within approximately 70–120% are generally considered acceptable, particularly when measurement uncertainty and counting statistics are taken into account. In the present study, the majority of recovery values fall within the narrower range of 80–110%, with overall mean recoveries close to 100%, indicating satisfactory chemical separation efficiency. Although one sample exhibited slightly lower recovery and two samples marginally exceeded 110%, no systematic trend of under- or over-recovery was observed. The overall distribution of recovery values therefore demonstrates adequate radiochemical control and supports the robustness of the analytical method.

Repeatability

Repeatability was evaluated through repeated measurements of IAEA-385 under identical analytical conditions. The control charts presented in Figures 2, 3, and 4 show the measured activities of ^{234}U, ^{235}U, and ^{238}U, respectively. The close agreement of successive measurements confirms method repeatability.

Although several measurements appear below the mean, all results remain within $\pm 2\sigma$ control limits and none exceed $\pm 3\sigma$ limits. For low-activity isotopes such as ^{235}U, measurement variability is strongly influenced by Poisson counting statistics, where the variance is equal to the mean count rate (Knoll 2010). Under low-count conditions, relative uncertainty increases as $1/\sqrt{N}$, which may

produce apparent clustering or wider dispersion without indicating systematic bias. The data therefore satisfy statistical control criteria.

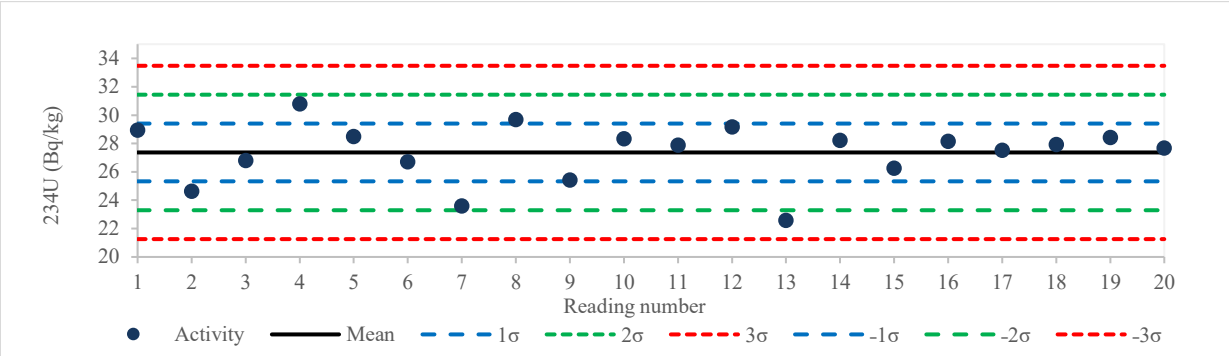

Figure 2 ^{234}U Radioactivity (Bq/kg) measured in IAEA-385

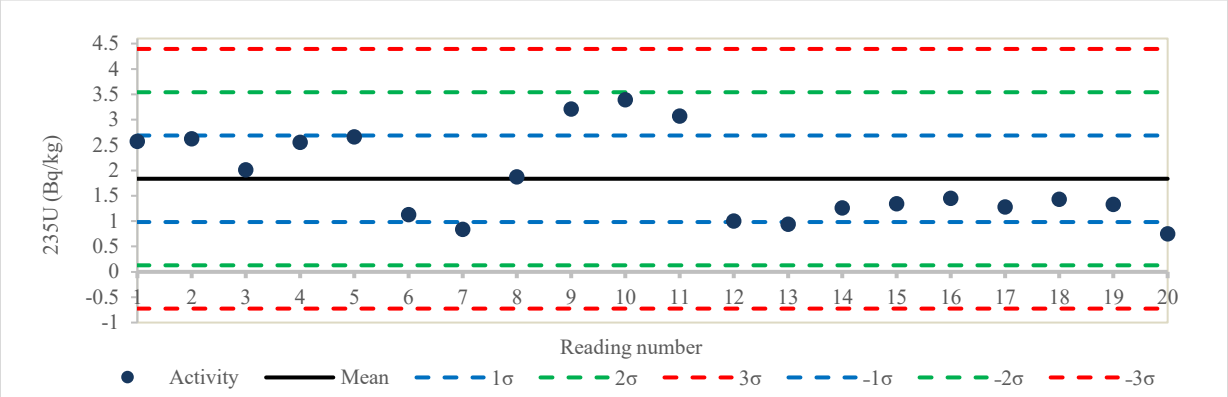

Figure 3 ^{235}U Radioactivity (Bq/kg) measured in IAEA-385

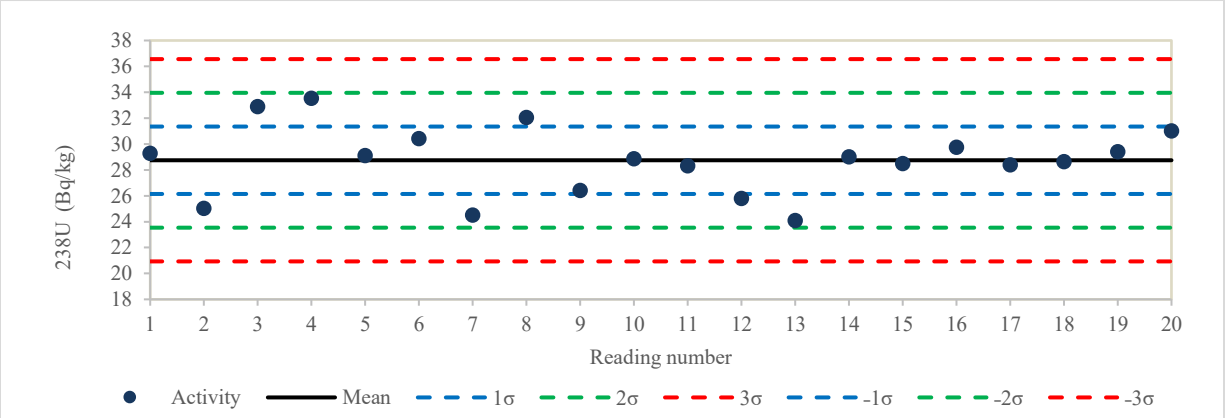

Figure 4 ^{238}U Radioactivity (Bq/kg) measured in IAEA-385

Robustness

The method's robustness was demonstrated through consistent performance across different CRMs. The performance of this method using IAEA-385 has been discussed under the accuracy parameter. The u-scores obtained for IAEA-384, as shown in Table 2, were 0.38, 0.78, and 0.72 for ^{234}U, ^{235}U, and ^{238}U, respectively, demonstrating statistically acceptable agreement with certified values and confirming the reliability of the radiochemical separation procedure across different environmental matrices.

Ruggedness

While robustness focuses on internal factors (such as sample composition) that affect method performance, ruggedness assesses how well a method performs across variations introduced by external factors. These conditions can include different laboratories, different analysts, different instruments, reagent lots, elapsed assay times, temperatures, and days.

The ruggedness of the method was assessed using CRM IAEA-385 by comparing results obtained independently by three analysts (TMZ, NAZ, and FTN). The detailed inter analyst results are presented in Table 3. The calculated u-scores for all analysts were below 1.64, demonstrating agreement within acceptable limits and confirming the method's reproducibility across operators.

Table 3 Uranium radioactivity value reported by different analysts

No of replicates	**^{234}U lab value (Bq/kg)**		
	Analyst TMZ	**Analyst NAZ**	**Analyst FTN**
1	28.23±3.62	28.96±4.4	32.28±3.93
2	26.26±3.16	24.64±3.85	32.25±4.12
3	28.16±3.29	28.49±4.49	31.82±3.93
4	27.52±3.85	26.8±4.43	32.1±3.81
5	27.93±3.99	28.35±5.31	31.68±3.83
6	28.44±4.26	29.18±5.25	25.68±3.71
7	27.68±4.11	25.42±4.79	
Mean (Bq/kg)	**27.75±3.75**	**27.41±4.65**	**30.97±3.89**
U score	**0.14**	**0.04**	**0.93**
Z score	**0.75**	**0.11**	**1.45**

No of replicates	**^{235}U lab value (Bq/kg)**		
	Analyst TMZ	**Analyst NAZ**	**Analyst FTN**
1	1.26±0.96	2.57±1.2	2.38±0.91
2	1.34±1.01	2.62±1.17	2.03±0.94
3	1.45±0.77	2.66±1.27	2.17±0.9
4	1.28±1.7	2.01±1.2	2.06±0.79
5	1.43±1.55	3.39±1.94	1.29±0.73
6	1.33±1.69	1±1.42	1.06±0.89
7	0.75±1.08	3.21±1.79	

Mean (Bq/kg)	**1.26±1.25**	**2.49±1.43**	**1.83±0.86**
U score	**0.08**	**0.79**	**0.54**
Z score	**0.41**	**1.42**	**0.89**

No of replicates	**^{238}U lab value (Bq/kg)**		
	Analyst TMZ	**Analyst NAZ**	**Analyst FTN**
1	29±3.73	29.27±4.4	33.36±4.04
2	28.5±3.27	25.02±3.85	24.93±3.47
3	29.74±3.49	29.1±4.51	25.19±3.35
4	28.38±3.91	32.9±5.07	25.25±3.2
5	28.65±4.1	28.85±5.29	25.38±3.29
6	29.41±4.4	25.8±4.76	25.15±3.63
7	31.01±4.37	26.41±4.84	
Mean (Bq/kg)	**29.24±3.90**	**28.19±4.67**	**26.54±3.50**
U-score	**0.04**	**0.25**	**0.77**
Z score	**0.17**	**0.45**	**0.85**

CONCLUSION

The developed method for the determination of ^{234}U, ^{235}U, and ^{238}U in environmental samples demonstrated satisfactory performance with respect to the evaluated validation parameters. Evaluation using IAEA-certified reference materials (IAEA-385 and IAEA-384) confirmed acceptable selectivity, accuracy, precision, repeatability, and robustness under the applied conditions. The calculated u-scores and z-scores met the established acceptance criteria, indicating no statistically significant deviation from the certified values and confirming the method's accuracy and reliability. Precision assessment based on RSD values demonstrated consistent performance, with variability for ^{235}U attributable to counting statistics associated with its lower activity concentration. The method's ruggedness was further verified through consistent results obtained by different analysts. Although the present validation demonstrates strong analytical performance, additional studies are recommended to further evaluate parameters such as LOD, LOQ, and extended robustness testing. Overall, the validated method provides a reliable and standardized approach for uranium isotope determination in environmental matrices, supporting environmental monitoring and radiological assessment.

ACKNOWLEDGEMENT

The authors would like to express their sincere appreciation to the staff of the Radiochemistry and Environment Group, Waste Technology and Environmental Division, Malaysian Nuclear Agency, for their continuous support and assistance throughout this study. The authors also thank Ms. Nazirrah Mohd Nazry Rethinasamy and Ms. Fatin Ayunie binti Rozi from Universiti Kebangsaan Malaysia for their valuable contributions to sample preparation and laboratory work. Their dedication and commitment were instrumental in the successful completion of this research.

REFERENCES

EPA. (2006). Technical Report on Technologically Enhanced Naturally Occurring Radioactive Materials from Uranium Mining Volume 1 : Mining and Reclamation Background. U . S . Environmental Protection Agency Office of Radiation and Indoor Air Radiation Protection Divisi. Vol. 1

Eurachem. (1998). *The Fitness for Purpose of Analytical Methods*. *Eurachem Guide, ISBN: 0-94948926-12-0* http://www.eurachem.org/images/stories/Guides/pdf/valid.pdf.

Gaburo, J.C., Todo, A.S., Taddei, M.H.T. & Silva, N.C. (2006). Implementation of alpha-spectrometry for uranium isotopes in excreta samples. *Journal of Radioanalytical and Nuclear Chemistry 269*(2): 499–503.

Guérin, N. & Dai, X. (2015). An emergency bioassay method for 210Po in urine. *Applied Radiation and Isotopes 103*: 179–184. http://dx.doi.org/10.1016/j.apradiso.2015.06.013.

Horwitz, E. P., Dietz, M. L., & Nelson, D. M. (1992). Extraction chromatography of actinides and selected fission products: Principles and achievement of selectivity.*Analytica Chimica Acta*, 266, 25–37.

Jia, G., Belli, M., Sansone, U., & Rosamilia, S. (2002). Determination of uranium isotopes in environmental samples by alpha-spectrometry. *Journal of Radioanalytical and Nuclear Chemistry*, 253(3), 395–406.

Horwitz, E. P., Chiarizia, R., Dietz, M. L., Diamond, H., & Nelson, D. M. (1993). Separation and preconcentration of actinides from acidic media by extraction chromatography. *Analytica Chimica Acta*, 281, 361–372.

IAEA. (1997). Environmental impact assessment. *Environmental impact assessment for uranium mine, mill and in situ leach projects* (November): 253–283.

IAEA. (1997). *Measurement of Radionuclides in Food and the Environment: A Guidebook.* Technical Reports Series No. 295 (Rev. 1). Vienna: IAEA. ISBN: 92-0-125297-6

IAEA. (2005). Environmental contamination from uranium production facilities and their remediation. *Environmental Contamination from Uranium Production Facilities and their Remediation* (February): 11–13.

International Organization for Standardization. (2015). Statistical methods for use in proficiency testing by interlaboratory comparison (ISO Standard No. 13528:2015). https://www.iso.org/standard/56125.html

Knoll, G. F. (2010). *Radiation Detection and Measurement* (4th ed.). Hoboken, NJ: John Wiley & Sons. ISBN: 978-0-470-13148-0

Magnusson, B. & Örnemark, U. (2014). The Fitness for Purpose of Analytical Methods: A Laboratory Guide to Method Validation and Related Topics. *Eurachem* ISBN 978-91-87461-59-0.

NATA. (2006). Technical Note 17-Guidelines for the validation and verification of chemical test methods. *National Association of Testing Authorities, Australia (NATA)*. Australia.

National Nuclear Data Center (NNDC). (2023). *NuDat 3.0 Nuclear Structure and Decay Data.* Brookhaven National Laboratory, Upton, NY, USA. Available at: https://www.nndc.bnl.gov/nudat3/. Accessed: 20 February 2026.

Rambla-Alegre, M., Esteve-Romero, J. & Carda-Broch, S. (2012). Is it really necessary to validate an analytical method or not? That is the question. *Journal of Chromatography A 1232*: 101–109. http://dx.doi.org/10.1016/j.chroma.2011.10.050.

Sushila Dagadu Chavan & Deepa Mahendra Desai. (2022). Analytical method validation: A brief review. *World Journal of Advanced Research and Reviews 16*(2): 389–402.

Thompson, M., Ellison, S.L.R. & Wood, R. (2006). *The International Harmonized Protocol for the Proficiency Testing of Analytical Chemistry Laboratories.* Pure and Applied Chemistry, 78(1), 145–196.

Jurnal Sains Nuklear Malaysia, 2025, 37(No. 2): 34 – 43
ISSN: 2232-0946

A SEDIMENT CONTRIBUTION FROM DIVERSITY OF LAND USE TO THE SEMBRONG CATCHMENT AREA, KLUANG, JOHOR, MALAYSIA

Jalal Sharib@Sarip[1*], Dainee Nor Fardzila Ahmad Tugi[1], Mohd Tarmizi Ishak[1] and Mohd Izwan Abdul Adziz[1]

[1*]Radiochemistry and the Environment Group
Waste and Environment Technology Division
Malaysian Nuclear Agency,
Bangi, 43000 Kajang, Selangor, Malaysia
*Corresponding author email: jalal@nm.gov.my

ABSTRACT

Soil erosion and sedimentation are significant environmental concerns affecting freshwater reservoirs. This study investigates the sources of sediment contributing to the Sembrong catchment in Kluang, Johor, Malaysia, by analysing sediment samples from various land uses during both dry and wet seasons. The study area includes the Sembrong Reservoir (7.76 km², 24.84 million m³ capacity) and a catchment of approximately 130 km². The Compound-Specific Stable Isotope (CSSI) technique, using $\delta^{13}C$ as non-radioactive tracer was applied to identify sediment sources. Results indicate that banana plantations are the dominant sediment contributors, accounting for 41% of the total sediment load, compared to 11% from recreational areas, with no significant seasonal variation. These findings highlight the effectiveness of CSSI in tracing sediment sources and emphasize the need for targeted erosion control in agricultural landscapes.

Keywords: Sediment sources, Stable Isotopes, Compound-Specific Stable Isotopes (CSSI), Sembrong catchment

ABSTRAK

Hakisan tanah dan pemendapan adalah merupakan satu kebimbangan ketara alam sekitar yang menjejaskan takungan air tawar. Kajian ini adalah merupakan siasatan terhadap sumber sedimen yang menyumbang kepada tadahan Sembrong di Kluang, Johor, Malaysia, dengan menganalisis sampel sedimen daripada pelbagai guna tanah semasa musim kering dan basah. Kawasan kajian adalah termasuk Takungan Sembrong (7.76 km², kapasiti 24.84 juta m³) dan kawasan tadahan kira-kira 130 km². Teknik Isotop Stabil Khusus Kompaun (CSSI), menggunakan $\delta^{13}C$ sebagai penyurih bukan radioaktif telah digunakan untuk mengenal pasti sumber sedimen. Keputusan menunjukkan bahawa ladang penanaman pisang adalah penyumbang sedimen yang dominan, menyumbang 41 % daripada jumlah bebanan sedimen, berbanding 11 % dari kawasan rekreasi tanpa perubahan musim yang ketara. Penemuan ini memperkukuhkan keberkesanan CSSI dalam mengesan sumber sedimen dan menekankan bahawasanya keperluan kawalan hakisan yang disasarkan dalam landskap pertanian.

Kata kunci: *Sumber sedimen, Isotop Stabil, Isotop Stabil Khusus Kompaun (CSSI), Tadahan Sembrong*

INTRODUCTION

Soil erosion and sedimentation are significant environmental issues that frequently disrupt tropical ecosystems. These processes lead to nutrient loss from the soil surface, reduced soil water retention, decreased fertility, and inhibited plant growth (Vásquez-Méndez et al., 2010). Soil erosion occurs when natural forces such as water, wind, waves, and glaciers remove soil from the Earth's surface. Major contributing factors include heavy rainfall, continuous water flow after storms, tornadoes, sandstorms, and coastal wave action. These forces accelerate soil erosion, leading to widespread environmental and economic consequences. One of the most pressing concerns is the economic impact of soil erosion on a global scale. Beyond the recurring erosion process itself, human activities have significantly intensified the problem—land degradation due to deforestation and unsystematic land clearing for agriculture and development has increased erosion rates by 10 to 40 times worldwide.

In Malaysia, land clearing, particularly through deforestation within climatic vegetation ecosystems, continues to significantly alter the hydrological balance. This, in turn, leads to soil erosion, causing rivers to become polluted with silt and insoluble elements. As sediment accumulates, the riverbed becomes shallower, disrupting aquatic ecosystems and increasing the risk of flooding due to excessive water overflow. Local studies on soil erosion have primarily focused on slope-scale or small river basin areas, often employing soil erosion models. Globally, extensive research has explored the interaction of geomorphological factors in catchment areas concerning soil erosion and land degradation (Nyssen et al., 2005). Excessive soil erosion, especially following heavy rainfall, has caused numerous environmental issues, including reduced agricultural productivity due to soil degradation, sedimentation of waterways, and ecological collapse from nutrient depletion. Farmers often compensate for nutrient loss by increasing fertilizer use, which further impacts the environment. Research has identified rainwater as the primary contributor to soil degradation, accounting for approximately 84% of cases. Soil erosion remains a critical global environmental challenge due to the energy exerted by raindrops, which dislodge and fragment soil particles upon impact. This process intensifies when rain persists over extended periods, continuously eroding the soil surface and accelerating land degradation.

Over the last few decades, numerous publications have explored the various applications of Fallout Radionuclides (FRNs), particularly ^{137}Cs, in soil erosion studies (e.g., Ritchie & McHenry, 1990; Walling & Quine, 1990, 1993; Zapata, 2002; Ritchie et al., 1974). ^{137}Cs has proven to be an effective diagnostic tool for fingerprinting sediment sources (e.g., Wallbrink et al., 1998; Motha et al., 2003) and is widely used as a sediment tracer (Ritchie & McHenry, 1990; Zapata, 2002). Several local studies have also utilized the FRNs approach to determine erosion and deposition rates, particularly in the short and medium term. For instance, Jalal et al. (2019, 2020, 2021) applied ^{7}Be and ^{137}Cs tracers to assess seasonal variations in erosion and deposition at the Timah Tasoh study site, Perlis. Additionally, Jalal et al. (2020, 2021) used ^{7}Be to analyse soil penetration rates across rainy and dry seasons at a study site in Bangi, Selangor. These studies demonstrate the effectiveness of FRNs as tracers in successfully identifying erosion and sedimentation rates over short and medium timescales.

However, the use of Fallout Radionuclides (FRNs) alone cannot fully identify the source of sediment transported into the catchment area. To address this limitation, a study using the Compound Specific Stable Isotope (CSSI) approach was conducted in the Timah Tasoh catchment area, Perlis, to trace sediment sources (Jalal et al., 2020) in relation to soil erosion and sedimentation. The relationship between sediment sources, mobilization, transport,

deposition, storage, and yield at the basin outlet can be highly complex, especially when sediment storage equals or exceeds sediment export (cf. Trimble, 1983; Phillips, 1992; Walling et al., 2000). Sediment budgets provide valuable insights into sediment sources, sinks, and yields (Golosov et al., 1992; Reid & Dunne, 1996; Walling, 2000; Walling et al., 2001) and are increasingly recognized as essential tools for sediment management (Walling & Collins, 2008). To support this study, sediment samples collected after heavy rainfall were processed at the Radiochemical and Environmental Group Laboratory (RAS), Nuclear Malaysia, for pre-treatment before analysis. The organic composition of CSSI markers was analysed using Gas Chromatography Mass Spectrometry (GC-MS) and Inductively Coupled Plasma Mass Spectrometry (ICP-MS), both of which are suitable for detecting fatty acid content in environmental samples. These fatty acids, derived from decomposed plant material in sediment deposits after flood events, serve as environmental forensic indicators to quantify sediment contributions and trace their sources.

This study aims to determine the sources of soil erosion and assess sediment contributions from various agricultural activities and land uses within the catchment area using the CSSI approach.

MATERIAL AND METHODOLOGY

Study area

The Sembrong Reservoir is one of the important ecosystems in Peninsular Malaysia since the 1960s and it has evolved from a natural ecosystem to a human-dominated one. The Sembrong catchment is located in Kluang, Johor between latitudes 3°26′42″ to 3°26′42″ N and longitudes 102°54′18″ to 102°55′54″E. The morphology provides significant information about the physical characteristics of the reservoir (Table 1). The freshwater reservoir area is 7.7547 km^2 with an estimated storage capacity of 24.84 million m^3, while the catchment area is about 130 km^2. Over the years, land use has changed dramatically, with agricultural activity increasing from 8% in 1984 to 82% in 2014 around the study site (Figure 1).

A total of 30 soil surface samples were taken from 6 sampling stations. All samples were collected and mixed in a bucket using a metal scraper hand tool (Figure 2). It is important that the sample is well mixed to ensure it accurately represents the site. The combined sediment samples were t transported to the Radiochemistry and Environment Group Laboratory (RAS), Block 23, Nuclear Malaysia for further processing. Each core sample was dried in an oven at a temperature of 45- 60 until a constant dry weight was achieved. The dried samples were then finely ground and sieved at 2 mm before undergoing ^{13}C analysis. The preparation procedure involved converting fatty acids and fatty acid derivatives into Fatty Acid Methyl Ester (FAMEs) to ensure that the ^{13}C analysis analysis provided reliable results for the study.

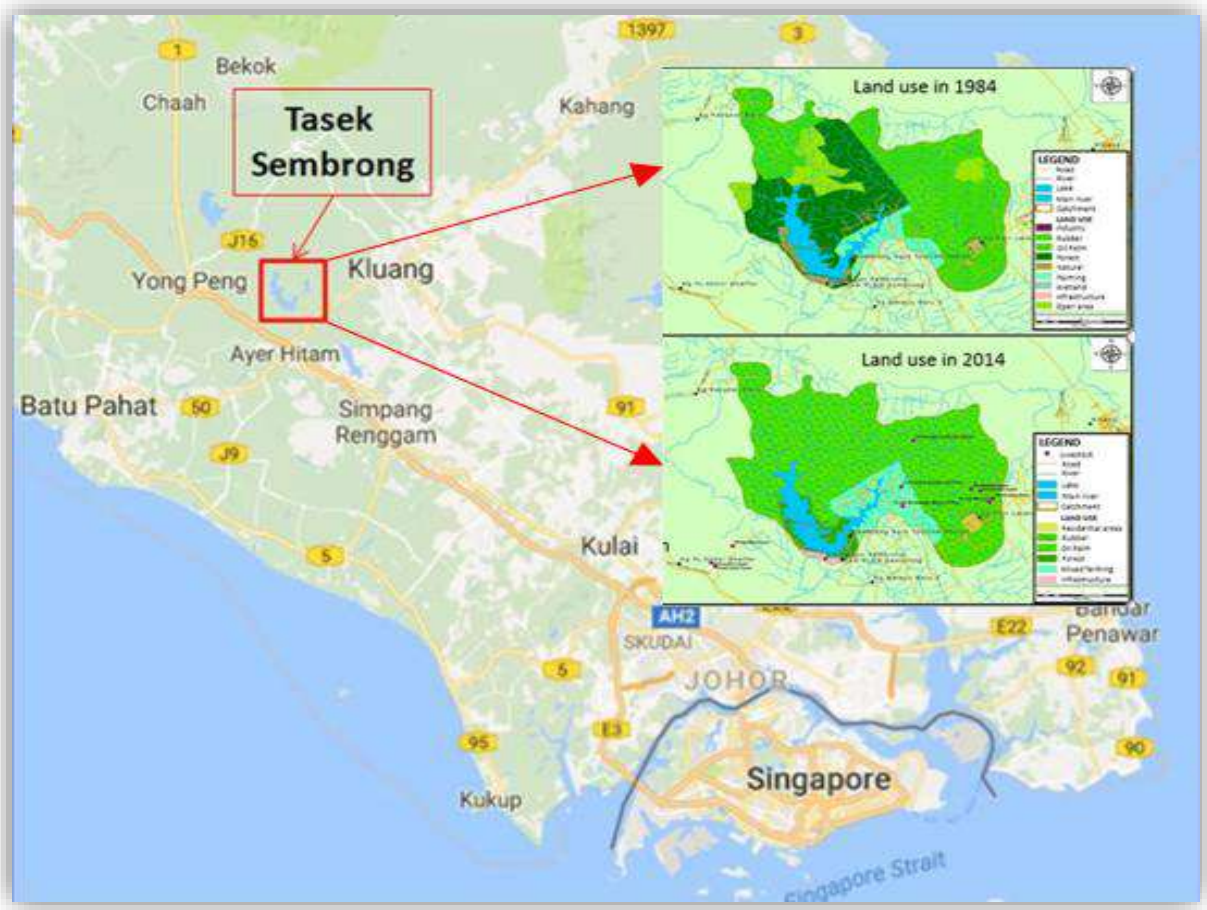

Figure 1: Study site in different land use in Sembrong catchment, Kluang, Johor

Table 1: The physical characteristics of Sembrong catchment

No.	Parameter	Value
1.	Lake area (km^2)	7.7547
2.	Volume (km^3)	36
3.	Maximum depth (m)	7
4.	Mean depth (m)	3.2
5.	Mean slope (%)	4
6.	Height (m)	9
7.	Catchment's area (km^2)	130
8.	Storage capacity (million m^3)	24.84
9.	Spillway	Concrete Fixed Ungated Ogee Crest

Figure 2: A metal scraper hand tool for CSSI sampling

Preparation for $\delta^{13}C$ analysis of fatty acids

The solvent used in this procedure is a high purity Dichloromethane (DCM) , specifically High-Performance Liquid Chromatography (HPLC) grade or double-distilled DCM Grade High Performance Liquid Chromatography (HPLC) or double distillation and Accelerated Solvent Extractor (ASE) cells must Accelerated Solvent Extractor (ASE) cells must be thoroughly cleaned beforehand to prevent contamination and ensure accurate analysis results.Shaker extraction typically takes 24 hours, while ultrasonic extraction requires 6–8 hours. Before extraction, the sample must be soaked in 100 mL of DCM inside a 250 mL Erlenmeyer flask with a ground-glass stopper. The sample must then be filtered to remove soil particles. The solvent is reduced to dryness in a 100 mL round-bottom flask using a Büchi evaporator and should be stored for recycling through the distillation system.

Fatty acid derivatives to fatty acid methyl esters (FAMEs)

The dry extract should be transferred from a 100 mL round-bottom flask to a 10 mL Kimax screw-cap reaction tube using 2 mL of DCM with a cleaned Pasteur pipette. Next, add 2 mL of 5% boron trifluoride (BF_3) in methanol to the Kimax tube, securely screw the cap, and place the tube in a test tube rack inside a fan oven at 70°C for 20 minutes. After heating, add 2 mL of a hexane/DCM mixture (4:1) to each Kimax tube, screw the cap tightly, and mix using a vortex mixer for 2 minutes. The hexane content is then reduced to dryness in an aluminum heating

block at 40°C under a gentle flow of dry nitrogen, directed onto the solvent surface via a vertically positioned stainless-steel needle. Finally, the processed vials are sent to an analytical laboratory for the $\delta^{13}C$ FAMEs measurement.

Compound Specific Stable Isotope (CSSI) analyses

Methyl groups ($-CH_3$) added to fatty acids to produce fatty acid methyl esters (FAMEs) will have different isotopic values than fatty acids; therefore, the isotopic signature of FAMEs must be corrected to account for this addition. Although the correction for a single methyl group is relatively small, it must be applied to every fatty acid in every sample. This correction can be efficiently performed using a simple equation in a in a spreadsheet (Equation 1).

$$\delta^{13}C_{FA} = \frac{\delta^{13}C_{FAME} - (1 - X)\delta^{13}C_{Methanol}}{X} \quad (1)$$

In this equation, FA represents a fatty acid, and X is the fractional contribution of the fatty acid (FA) to its corresponding FAME. X is calculated by dividing the number of carbons in the FA molecule by the total number of carbons in the resulting FAME.
For example, stearic acid (C18:0) produces methyl stearate, which contains one additional carbon (19 carbon atoms in total). Thus, the X value for stearic acid is 18/19 or 0.9474.

The IsoSource Mixing Model software

Data processing for Compound Specific Stable Isotope (CSSI) analysis using the IsoSource mixing model and was conducted to identify the sources of sediment in the catchment area. The IsoSource mixing model is a software tool designed to calculate the range of possible proportional contributions of various sources to a mixture based on stable isotope data. It is particularly useful when the number of sources exceeds the number of isotopes + 1, making a unique solution impossible (Phillips & Gregg., 2003). Therefore, the IsoSource mixing model was designed for situations where there are too many sources. Although originally intended to study food webs, it is well suited to identifying and partitioning sources in sediment mixtures. Although the model can handle too many sources, running the model requires at least 3 sources. The model also requires at least 2 isotopes, one of which must be ^{13}C for bulk soil carbon. To use the model, data from potential source soils and sediments from the depositional zone must be compiled into a table including bulk $\delta^{13}C$ values and CSSI-corrected $\delta^{13}C$ values for Fatty Acids (FAs). A limitation of using IsoSource is that there must be a $\delta^{13}C$ value for each FA from each source soil as well as the sediment mixture. Obviously, a useful starting point is to take the $\delta^{13}C$ isotope values for bulk soil carbon and two fatty acids, oleic and palmitic acids, to test the level of discrimination.

RESULTS AND DISCUSSION

Data processing for Compound Specific Stable Isotope (CSSI) analysis using the Iso-Source Mixing model was conducted to identify the sources of sediment in the catchment area. The statistical approach produced multiple solutions, with mean histogram increments ranging from 0.0 to 1.0 for each source. The model compared CSSI data from sediment sources with mixed sediment samples to determine their origins. To achieve this, potential sediment sources within the catchment were characterized, enabling comparisons based on stable ^{13}C isotopic properties measured in both sources and sediments. The CSSI analysis results provided insights into sediment contributions from different land uses across two seasons (Table 2 and Table 3). The highest sediment contribution originated from banana plantations, accounting for 36% and 41% of the total sediment deposition in both seasons, particularly at Station 12. This high contribution is likely due to intense soil erosion following floods caused by heavy rainfall.

Table 2: Sediment contribution results from different land uses (dry season) estimated using the Iso-Source mixing model (Philips & Gregg ., 2003)

Station	Land use	Contribution	Remarks (matrix of sample)
Station 16	Palm oil plantation	0.19	Sediment
Station 19 + 20	Forest	0.21	Sediment
Station 12	Banana Plantation	0.36	Sediment
Station 14	Modern agriculture	0.13	Sediment
Station 5	Recreation area	0.11	Sediment
Total		1.0	

Table 3: Sediment contribution results from different land uses (wet season) estimated using the Iso-Source mixing model (Philips & Gregg ., 2003)

Station	Land use	Contribution	Remarks (matrix of sample)
Station 16	Palm oil plantation	0.16	Sediment
Station 19 + 20	Forest	0.18	Sediment
Station 12	Banana Plantation	0.41	Sediment
Station 14	Modern agriculture	0.15	Sediment
Station 5	Recreation area	0.10	Sediment
Total		1.0	

Furthermore, the absence of adequate ground cover between banana plants exacerbated surface erosion, especially after heavy rains. Despite this, statistical analysis indicated no significant difference in sediment contribution between the two seasons at this station ($p > 0.05$). In contrast, Station 14, a modern agricultural area, exhibited the second-lowest sediment contribution (13%), significantly lower than that of Station 12. This can be attributed to well-managed land use practices, including closed-crop systems with plastic coverings, which reduce rainwater infiltration and minimize soil erosion. The second and third largest sediment contributions came from Stations 19+20 (Forest) and Station 16 (Palm Oil Plantation), with values showing minimal seasonal variation. The dry season led to a slight increase in sediment

deposition due to heavy rainfall in November 2019, particularly at Stations 19+20 (Forest). This rainfall event likely triggered soil erosion and subsequent sediment transport.

However, the presence of extensive vegetation cover in forests and palm oil plantations played a crucial role in mitigating erosion compared to the banana plantation. Large leaf surface areas and forest floor coverage reduced rainfall impact and runoff, resulting in lower sediment transport. Station 5, a recreational area, had the lowest sediment contribution throughout the study period for both seasons, with values of 10% and 11%, respectively. The minimal erosion at this site can be attributed to the presence of well-maintained ground cover, including managed grazing systems and controlled replanting of high grasses.

Overall, sediment contribution patterns observed in this study align with findings by Zullyadini et al. (2013) in Timah Tasoh, Perlis. However, the erosion and sedimentation rates remain lower than those reported for large-scale agricultural areas in the United States (6 Mg ha−1 yr−1) and Northeast China (15 Mg ha−1 yr−1) (Mark A.N. et al., 2017).

CONCLUSION

This study identified Station 12 (banana plantation) as the highest contributor to sediment entering the Sembrong catchment, while Station 5 (recreational area) had the lowest contribution. However, the difference between these values was not statistically significant ($p > 0.05$). Station 14 (modern agriculture) recorded the second-lowest sediment contribution, attributed to well-organized land use practices, including closed-crop systems (plastic coverings) and widespread cover crops. These measures effectively reduced soil erosion, highlighting the importance of structured agricultural practices in minimizing sediment deposition. Overall, this study successfully identified the primary sediment contributors from various land uses within the catchment area across both study seasons. However, no significant seasonal differences were observed.

In conclusion, the Compound Specific Stable Isotope (CSSI) approach using the IsoSource Mixing Model proved to be a valuable tool for identifying sediment sources in erosion-prone areas, particularly in highly agricultural regions. Future research should expand its application to other catchments across Peninsular Malaysia and the rest of the country to further enhance sediment source tracking and erosion management strategies.

ACKNOWLEDGEMENTS

The author expresses sincere gratitude to the members of the IAEA/RCA RAS 5084: Assessing and Improving Soil and Water Quality to Minimize Land Degradation and Enhance Crop Productivity Using Nuclear Techniques project for their invaluable cooperation and assistance. Special thanks are extended to those directly and indirectly involved in sampling, preparation, and analysis throughout the study. Their contributions ensured the smooth execution and successful completion of this research. The author also appreciates the continued support in sharing research findings for future publications.

CONFLICTS OF INTEREST

The authors declare no conflict of interest.

REFERENCES

Golosov, V.N., Ivanova, N.N., Litvin, L.F. and Sidorchuk, A.Yu. (1992). Sediment budget in river basins and small river aggradation. *Geomorphologiya,* Vol.4, pp. 62-71 (in Russian)

Jalal, S., Zainudin, O., Dainee, N.F.A.T (2019). Determination of Medium-Term Soil Erosion and Sedimentation Rates in Two Seasons, International Journal of Agriculture, Forestry and Plantation, Vol. 8 (June) ISSN 2462-1757:120-127

Jalal, S., Zainudin, O., Dainee, N.F.A.T., Noor Fadzilah,Y., Mohd,T.I .,Mohd ,I.A.A., (2020). The Compound Specific Stable Isotope (CSSI) values in Timah Tasoh Soil Erosion Study, International Journal of Agriculture, Forestry and Plantation, Vol. 9 (Feb) ISSN 2462-1757:1-10

Jalal, S., Dainee, N.F.A.T., Noor Fadzilah,Y., Mohd,T.I .,Mohd ,I.A.A., (2020). The Depth Distribution of Beryllium 7 In the Soil Study, International Journal of Agriculture, Forestry and Plantation, Vol. 9 (Feb) ISSN 2462-1757:11-18

Jalal, S., Zainudin, O., Dainee, N.F.A.T., Noor Fadzilah,Y., Mohd,T.I .,Mohd ,I.A.A., (2020). The Short-Term Erosion Rates in Different Land Use Study, International Journal of Agriculture, Forestry and Plantation, Vol. 9 (Feb) ISSN 2462-1757:19-27

Jalal, S., Zainudin, O., Dainee, N.F.A.T., (2021). Quantifying the Relative Amounts of Soil Erosion and Sedimentation in Different Land Use, ASM Sc.J.,16, Special Issue 1, 2021 for SCIEMATHIC 2019, 172- 179

Jalal, S., Zainudin, O., Dainee, N.F.A.T., Nurrul , A.M.J., Nooradilah, A., Mohd, T.I., (2021). The Beryllium-7, ^{7}Be Depth Penetration in Two Seasons Study at Timah Tasoh, Perlis, ASM Sc.J.,16, Special Issue 1, 2021 for SCIEMATHIC 2019, 180-186

Mark A.Net al., (2017) Natural and anthropogenic rates of soil erosion , International Soil and Water Conservation Research Volume 5, Issue 2, Pages 77-84 Tamura, T. 1964. Selective sorption reactions of ^{137}Cs with soil mineral. Nucl. Saf. 5: 262-268

Motha, J.A., P.J. Wallbrink, P.B. Hairsine, and R.B. Grayson. (2002). Tracer properties of eroded sediment and source material. Hydrological Processes 16:1983-2000

Nyssen, J., Vandenreyken, H., Poesen, J., Moeyersons, J., Deckers, J., Mitiku, H., Salles, C., Govers, G., (2005). Rainfall erosivity and variability in the Northern Ethiopian Highlands. Journal of Hydrology 311, 172-178.

Phillips JD. (1992). The source of alluvium in large rivers of the lower Coastal Plain of North Carolina. Catena 19: 59–75.

Phillips, D. L. and Gregg, J. W. (2003). Source partitioning using stable isotopes: coping with too many sources. Oecologia, 136: 261 – 269.

Reid, L. R., Dunne, T. (1996). *Rapid Evaluation of Sediment Budgets*. Catena special publication (Geo-ecology Report). Catena Verl. GMBH Germany

Ritchie J.C. and McHenry J.R. (1974). Fallout ^{137}Cs: A tool in conservation research. *Journal of water and Soil Cultivation*. 30, 283-286

Trimble, S. W. (1983). A sediment budget for Coon Creek basin in the Driftless area, Wisconsin, 1883–1977. Am. J. Sci. 283: 454– 474.

Vásquez-Méndez R, Ventura-Ramos E, Oleschko K, et al. (2010). Soil erosion and runoff in different vegetation patches from semiarid Central Mexico. Catena, 80: 162–169.CrossRef Google Scholar

Wallbrink, P.J., Murray, A.S. and Olley, J.M. (1998). Determining sources and transient times of suspended sediment in the Murrumbidgee River, New South Wales, Australia, using fallout ^{137}Cs and ^{210}Pb. Water Resour. Res., 34(4):879-887.

Walling D.E. and Quine T.A. (1990): Calibration of caesium-137 measurements to provide quantitative erosion rate data. *Land Degradation and Rehabilitation* 2: 161-175.

Walling DE, Collins AL (2008) The catchment sediment budget as a management tool. Environ Sci Policy 11: 136–143

Walling, D.E. and Quine, T.A. (1993). Use of Caesium-137 as a Tracer of Erosion and Sedimentation: Hand Book for the Application of the Cesium Technique. Overseas Development Administration Research Scheme R4579. Department of Geography, University of Exeter, UK.

Walling, D.E., A.L. Collins, H.M. Sichingabula and G.J.L. Leeks. (2001). Integrated assessment of catchment suspended sediment budgets: a Zambian example. Land degradation & development, 12, pp.387-415

Walling, D.E., A.L. Collins. (2000). Integrated assessment of catchment sediment budgets: a technical manual. University of Exeter, UK, 168 p.

Zapata, F. (ed.) (2002) Handbook for the Assessment of Soil Erosion and Sedimentation Using Environmental Radionuclides. Kluwer, Dordrecht.

Zullyadini A. R, Mohd. F.M, Mohamad.A. O & Wan. R.I. (2013). The Contribution of Riverbank Erosion to the Suspended Sediment Transport in Timah Tasoh Reservoir, Perlis, Geografi Vol 1, No 2, 17 – 29, Penerbit Universiti Pendidikan Sultan Idris

Jurnal Sains Nuklear Malaysia, 2025, 37(No. 2): 44 – 52
ISSN: 2232-0946

GAMMA IRRADIATION EFFECT ON PHOSPHATE SOLUBILIZING BACTERIA *ACINETOBACTER CALCOACETICUS*

Chong Saw Peng, Phua Choo Kwai Hoe, Ahmad Zainuri Mohd Dzomir, Norellia Bahari and Mariani Deraman

Agrotechnology and Bioscience Division,
Malaysian Nuclear Agency,
Bangi, 43000 Kajang, Malaysia.
Corresponding author: sawpeng@nm.gov.my

ABSTRACT

Phosphorus deficiency is a growing global issue on approximately 40% of cultivated land, primarily in tropical, acidic, and alkaline regions. This deficit, as a result of soil fixation, erosion, and phosphorus lag behind absorption, severely limits plant growth, crop yield, and soil fertility. While chemical fertilizers are used regularly to correct this situation, excessive use leads to environmental pollution. Alternatively, phosphate-solubilizing bacteria (PSB), such as Acinetobacter calcoaceticus, offer a biodegradable solution through the conversion of insoluble phosphorus to plant-accessible forms. This study explores the application of gamma irradiation, a mutagenesis technique that induces genetic alterations to improve the phosphate-solubilizing capability in the bacteria. The results showed from 931 bacteria colonies chosen after the irradiation treatment, 9.88% of bacteria strains showed a hypermorphic effect on the phosphate solubilization compared to the control, and 36.84% of bacteria strains showed hypomorphic effects. The distribution of hypermorphic bacteria strains across the phosphate solubilization index (SI) range was the higher SI range (3.1-3.5) was 8, the middle SI range (2.1-2.5) was 50, and the lower SI range (1.1-1.5) was 0. Among the 8 higher hypermorphic mutants, B346, B394, C92, C371, D20, D49, D96, and D100, only 3 mutant strains (C371, D20, and D100) showed statistical significance compared to control. This study has successfully produced several improved Phosphate-Solubilizing Bacteria (PSB) strains with strong potential for development as biofertilizers.

Keywords: Gamma irradiation, Phosphorus, Phosphate-solubilising bacteria, *Acinetobacter calcoaceticus*, Mutagenesis

INTRODUCTION

Phosphorus deficiency is one of the issues that is widely affecting agricultural lands across the globe. Phosphorus (P) is an essential macronutrient in plants. It is needed in plant photosynthesis, respiration, energy transport, and nucleic acid formation (Khan *et al*., 2023). According to Solangi *et al.* (2023), there is a possibility of around 40% of agricultural land being phosphorus deficient due to the immobilization or slow uptake of phosphorus ions from the soil into roots. About 10 million hectares of cultivated land, particularly in tropical, acid, and alkaline soils, are experiencing some degree of phosphorus deficiency in the form of low native phosphorus in soil, erosion and runoff, fixation, immobilization, and slowed phosphorus uptake, making the phosphorus unavailable for plant use (Sharmin *et al*., 2024). Phosphorus deficiency was very 0detrimental to agriculture by limiting plant growth and productivity, leading to poor yields of crops and ultimately poor soil fertility (Solangi *et al*., 2023). Farmers

will, therefore, be strongly obligated to apply enormous amounts of chemical fertilizers to offset the deficiency. Meanwhile, overuse of chemical fertilizers can lead to pollution of the environment (Bisht *et al.,* 2021).

Besides the use of chemical fertilizers, plant growth-promoting rhizobacteria (PGPR), such as phosphate-solubilizing bacteria (PSB), can convert insoluble phosphorus into plant-available forms. PSB is a class of beneficial bacteria that infects the roots and converts insoluble phosphorus into soluble forms that are taken up by plants directly (Zhang *et al.,* 2024). PSB occurs in *Pseudomonas, Bacillus, Rhizobium, Azotobacter, Enterobacter, Serratia, Burkholderia*, and *Acinetobacter* (Pan *et al.,* 2023). PSB from *Acinetobacter* sp. will be investigated in this study. *Acinetobacter calcoaceticus* is a non-motile, aerobic, Gram-negative rod. They are usually found in isolation from water or soil and are known to have phosphate solubilization potential (Wakako *et al*., 2014).

A. calcoaceticus in this study has been enhanced in the ability for phosphate solubilization through gamma irradiation technology. The method, known as mutagenesis, involves the exposure of PSB to gamma rays that are capable of making alterations to DNA or chromosomes and initiating genetic mutations artificially (Durland & Ahmadian-Moghadam, 2022). These mutations can lead to new characteristics that increase their ability to solubilize phosphate in the soil. Previous research proved that ionizing radiation is promising for improving the effectiveness of PSB. *Pseudomonas fluorescens* were gamma-ray irradiated (100 – 1000 Gy) and assayed for phosphate-solubilizing activity (Kuheli *et al*., 2003). The mutant strains showed 2-3 folds higher phosphate-solubilizing activity than that of the wild-type strains. Whilst Chaudhary *et al.* (2022) has examined the enhancement in phosphate solubilization of *Bacillus subtilis* by UV mutagenesis and a superior PSB mutant strain GCM11 was obtained. Recent study on the gamma irradiation of *Aspergillus niger*, a phosphate-solubilizing fungus has shown an increased citric acid yield and improved phosphate solubilization (Peng *et al*., 2022). Yang *et al.* (2022) found that ion beam irradiation of *Penicillium oxalicum* resulted in mutant strains exhibiting higher organic acid secretion and consequently, greater phosphate-solubilizing activity. These findings collectively suggest that induced mutation using ionizing radiation can effectively breed superior fungal strains with enhanced bio-fertilizing potential.

Gamma irradiation facility at Malaysian Nuclear Agency (Gamma Cell Biobeam GM8000, Germany), has been used for mutation induction on agriculture samples as well as on biological samples including bacteria and fungus. Gamma irradiation was chosen in the study because gamma rays can cause changes in the DNA or chromosome level, which may increase the production or activity of some enzymes and enhance the phosphate-solubilizing capability (Abozahra *et al.,* 2025). Besides, gamma irradiation can induce mutations that increase stress tolerance in PSB and make it more tolerant to environmental stresses (Mohamed *et al.,* 2021). Moreover, the mutated PSB may have improved root colonization in the rhizosphere and led to more effective phosphate solubilization (Elhaissoufi *et al.,* 2020). Ultimately, this proven method of inducing beneficial mutations in PSB allows for the development of enhanced biofertilizer strains, which can significantly boost soil fertility and phosphorus availability for optimal crop growth.

METHODOLOGY

Bacteria Strain

A. calcoaceticus bacteria used in the study was isolated from compost and soil at the Malaysian Nuclear Agency by Phua *et al.* (2019). The species identification was done using the 16S rRNA method by Chong *et al*. (2024).

Gamma Irradiation

Irradiation was conducted at Malaysian Nuclear Agency using gamma cell (Biobeam GM8000, Germany). Dose mapping was done before gamma irradiation was performed because the dose distribution inside any irradiation chamber is inherently non-uniform. Therefore, we used calibrated dosimeters placed at the sample position provides empirical confirmation that the bacteria actually receive the intended dose (Sharma *et al*., 2021). A radiosensitivity test previously conducted by Phua *et al.* (2024) established the lethal dose (LD50) of *Acinetobacter calcoaceticus* at 445.5 Gy. Accordingly, this dose was employed for gamma irradiation-mediated mutagenesis in the present study. The bacterial strains were cultured on nutrient agar (NA) plates in 90 mm diameter Petri dishes and were incubated at 28 ± 2 °C for 24 hours. The plate had roughly 50-100 single colonies per plate selected for further irradiation treatment. Ten plates were needed for each irradiation treatment, and the experiment was repeated 4 times. Culture plates were wrapped with aluminium foil and irradiated in the gamma cell. Fricke dosimetry was used to measure the doses absorbed during the treatment. The irradiated plates were placed at room temperature for 24 hours.

Colonies isolation

Approximately about 20-30 colonies were picked randomly from the plate. The single colony was picked using a sterile inoculating loop and then inoculated into a sterile test tube with 15 mL nutrient broth. The cultures were incubated in an incubator shaker at 28 ± 2 °C for 24 hours.

Screening for Phosphate-Solubilizing Strains

The qualitative screening method used and Potato Dextrose Agar (PDYA) media according to Silva *et al.* (2014). The media contains 39 g of potato dextrose agar, 1 g of yeast extract, and a calcium phosphate mixture of 50 mL of K_2HPO_4 (10% w/v) and 100 mL of $CaCl_2$ (10% w/v), which were separately autoclaved and added to the media before the resulting liquid medium was poured onto plates. Approximately 20 µL of irradiated bacterial suspension (>10^8 cfu/mL) was spotted on the PDYA agar plate. The non-irradiated *A. calcoaceticus* suspension was also spotted side-by-side with the sample as a control. The plates were incubated at 28 ± 2 °C for 6 days or until the expansion of the clear zone became stagnant. The expansion of the clear zone was quantified using the Solubilization Index (SI) (Mengesha & Legesse, 2024).

$$SI = \frac{\text{Colony Diameter + Halo Zone Diameter}}{\text{Colony Diameter}}$$

Colony Diameter: The bacterial or fungal colony diameter.
Halo Zone Diameter: The diameter of the clear zone around the colony where phosphate has been solubilized.

A higher SI indicates greater phosphate-solubilizing activity. Each bacterial culture had five replicates. ANOVA analysis with the means separated by Duncan's Multiple Range tests ($P \leq 0.05$) using One-Way ANOVA, SPSS (IBM Corp., 2021).

RESULTS AND DISCUSSION

The number of bacterial strains irradiated in the experiment was 931, which an adequate data to work with (Table 1). Approximately 92 strains (9.88%) showed a higher phosphate solubilization index (hypermorphic effect) than that in the control. This indicated that irradiation enhanced the capacity of the bacteria to solubilize the phosphate. However, 343 strains (36.84%) showed a hypomorphic effect on the phosphate solubilization index compared to the control, which means that irradiation reduced the capacity of the bacteria to solubilize the phosphate. This result show that irradiation would rather suppress or impair the activity of phosphate solubilization of *A. calcoaceticus* than enhance it where only 9.88% of the strains showed a positive effect. The low percentage indicated that only a few strains had their activity increased due to some genetic or physiological features that make them more susceptible to irradiation. This finding supports by a 2025 review on radiation mutagenesis states that most newly induced mutations are thought to be deleterious or neutral with no effects. Accordingly, mutations with beneficial effects on traits of interest are very rare (Geras'kin *et al.,* 2025)**.** The remaining strains (53.28%) showed no significant difference in solubilization activity compared to the control. These strains were not affected by irradiation, and the effects on their solubilization activity were not statistically detectable.

Table 1. The number of bacteria irradiated with gamma irradiation and the effect of the gamma-ray on the phosphate solubilization index (SI) of the sample.

Number of strains	Number of hypermophic strains	Percentage of hypermorphic strains (%)	Number of hypomorphic strains	Percentage of hypomorphic strains (%)
931	92	9.88	343	36.84

The results in Figure 1 showed that most hypermorphic mutant strains, 50 out of 92, fell in the SI range of 2.1–2.5, suggesting that irradiation typically induced a moderate enhancement in solubilization activity rather than extreme improvements. The second-highest number of hypermorphic mutant strains was 26 out of 92, falling in the SI range of 2.6–3.0. Approximately 8 strains were found in the higher SI range (3.1–3.5) and lower SI range (1.6–2.0). Only 8 strains fell in the 3.1–3.5 SI range, indicating that very high solubilization activity after irradiation was rare. These strains could be of interest for further study and potential biofertilizer applications as they represent the best-performing subset. The 8 strains in the 1.6–2.0 SI range showed only a slight improvement over the control, suggesting their response to irradiation was minimal. The absence of strains in the 1.1–1.5 SI range indicated that irradiation does not produce strains with very low solubilization activity among the hypermorphic group.

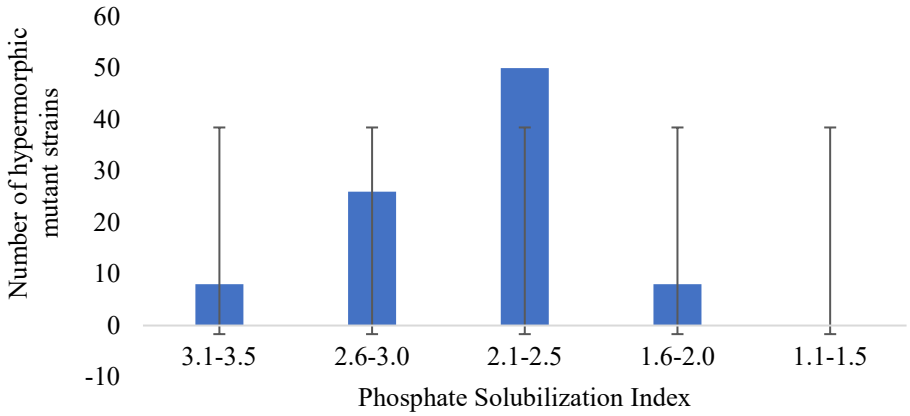

Figure 1. The number of hypermorphic *A. calcoaceticus* strains based on their phosphate solubilization index (SI) ranges (Premono *et al.,* 1996). SI>1: Indicates some level of phosphate solubilization. The higher SI reflects the greater phosphate-solubilizing activity. SI=1: No solubilization.

The eight strains with a higher SI range (3.1–3.5) from Figure 1 were repeated in the phosphate solubilization test with at least five replicates per strain on the PDYA medium. The clear zone around bacteria colonies on the PDYA medium was a key indicator of the phosphate-solubilizing activity of *A. calcoaceticus* (Fig. 2). The size of the clear zone reflects the efficiency of the bacteria in solubilizing insoluble phosphate compounds into soluble forms that plants can absorb. The expansion of the clear zone was quantified using the Solubilization Index (SI) (Mengesha & Legesse, 2024). Based on the results shown in Figure 3, the average SI values ranged from 2.59 (D49) to 2.79 (D20), indicating relatively close performance among the strains with no significant differential among them. Moreover, the variability in the SI ranged from 0.0927 to 0.2272 was generally low, indicating the data were robust and reproducible (Table 2).

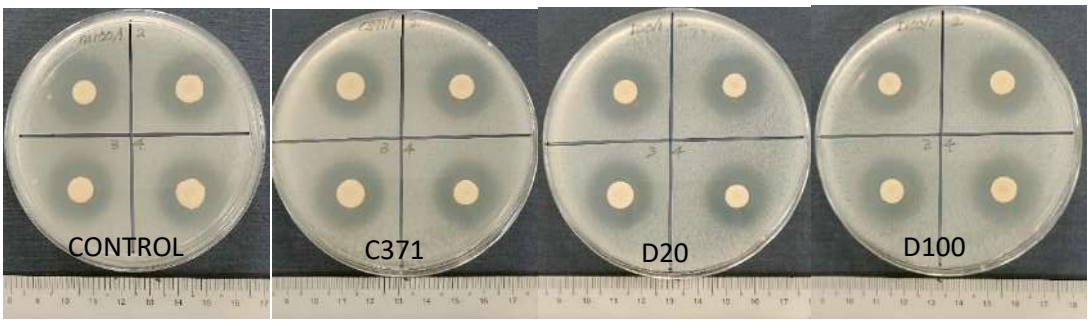

Figure 2. A phosphate solubilization clear zone appeared around the hypermorphic *A. calcoaceticus* strains (C371, D20, and D100) and the control strain on agar media.

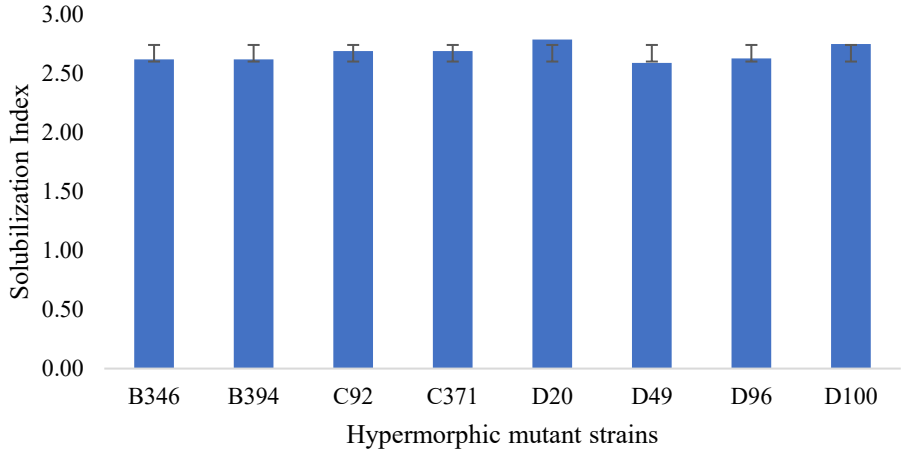

Figure 3. The hypermorphic mutant strains based on their phosphate solubilization index (SI) ranges (Premono *et al.,* 1996). The f-ratio value is 1.98446. The p-value is .118403. The result is not significant at $p < 0.05$.

The statistical significance (p-values) in Table 2 showed significant strains ($p<0.05$) C371, D20, and D100 with p-values 0.019953, 0.004327, and 0.010642, respectively. These strains exhibited statistically significant differences in SI compared to the control, indicating that they have higher phosphate-solubilizing activity. The remaining strains B346, B394, C92, D49, and D96 have p-values higher than 0.05, indicating their SI values were not significantly different. Among the significant strains, D20 was the most significant, standing out with the highest SI and the lowest p-value. However, C371, despite having a mid-range SI, shows very low variability and significance, making it a reliable candidate. Based on the results, D20, C371, and D100 were the most promising strains due to their statistical significance. These mutated phosphate-solubilizing bacteria strains have shown an enhancement in their ability to produce organic acids, enzymes, or metabolites that solubilize phosphate caused by gamma irradiation. Further investigation into their gene sequences at the molecular level is needed.

Table 2. The comparison between each potential mutated strain with the control SI (2.48) based on their average Selection Index (SI) (Premono *et al.,* 1996). Standard deviations and p-values were calculated using One-Way ANOVA with significance at the $p < 0.05$ level.

Potential mutated strains	Average SI	Standard Deviation	p-value	Significant at $p < 0.05$
B346	2.62	0.1409	0.154868	Not Significant
B394	2.62	0.1874	0.203302	Not Significant
C92	2.69	0.2272	0.087023	Not Significant
C371	2.69	0.0927	0.019953	Significant
D20	2.79	0.1383	0.004327	Significant
D49	2.59	0.1715	0.271801	Not Significant
D96	2.63	0.1498	0.120386	Not Significant
D100	2.75	0.1429	0.010642	Significant

CONCLUSION

Infertility of agricultural soils due to phosphate deficiency is a worldwide issue and causes a reduction in crop production. One solution to overcome this issue is to use phosphate-solubilizing bacteria as it can increase the phosphorus content in the soil and improve the soil condition in the long term. Mutagenesis using gamma irradiation was used in this study to develop new bacterial strains with enhanced characteristics, such as phosphate solubilization. These mutants exhibit greater phosphate solubilization activity than the original strain and can be further developed as biofertilizer products.

ACKNOWLEDGEMENT

This research was conducted under the Malaysian Nuclear Agency internal project (R&D-NM-21-67) and supported by the Forum for Nuclear Cooperation in Asia (FNCA) under the project Radiation Processing and Polymer Modification for Agricultural, Environment, and Medical Application (RPPM).

REFERENCES

Abozahra, M. S., Amin, M. A., Sarker, T. C., Abd-ElGawad, A. M., and Aboelezz, E. (2025). Molecular, biophysical, and biochemical studies on irradiated *Zea mays* seeds using various sources of gamma rays for dosimetrical applications. *Scientific Reports* Vol. 15, 9340. doi.org/10.1038/s41598-025-87531-5

Bisht, N. and Chauhan, P. S. (2021). Excessive and disproportionate use of chemicals cause soil contamination and nutritional stress. Soil contamination - threats and sustainable solutions. *IntechOpen*. doi:10.5772/intechopen.94593

Chaudhary, R., Nawaz, A., Fouillaud, M., Dufossé, L., Haq, Iu., and Mukhtar, H. (2022). Enhanced production of phytase through UV mutagenesis of *Bacillus subtilis*. *Food Science & Nutrition* 10, 3700–3709. DOI: 10.1002/fsn3.2967

Chong, S. P., Phua, C. K. H., Mohd-Dzomir, A. Z., Bahari, N., and Deraman, M. (2024). Pyrroloquinoline quinone (pqq) genes isolation in *Acinetobacter calcoaceticus.* In *Seminar R&D 2024, 27-29 August 2024, Bangi, Selangor, Malaysia*

Durland, J. and Ahmadian-Moghadam, H. (2022). Genetics, Mutagenesis. In: *StatPearls [Internet]*. Treasure Island (FL): StatPearls Publishing; 2025 Jan-. Available from: https://www.ncbi.nlm.nih.gov/books/NBK560519/

Elhaissoufi, Wissal., Khourchi, S., Ibnyasser, A., Ghoulam, C., Rchiad, Z., Zeroual, Y., Lyamlouli, K., and Bargaz, A. (2020). Phosphate solubilizing rhizobacteria could have a stronger influence on wheat root traits and above ground physiology than rhizosphere P solubilization. *Frontiers in Plant Science* Vol. 11. doi:10.3389/fpls.2020.00979

Geras'kin, S., Churyukin, R., and Kazakov, E. (2025). Application of ionizing radiation for crop improvement. *Planta* 262(3), 76. DOI: 10.1007/s00425-025-04796-w

IBM Corp. (2021). IBM SPSS Statistics for Windows, Version 28.0. Armonk, NY, IBM Corp.

Khan, F., Siddique, A. B., Shabala, S., Zhou, M., and Zhao, C. (2023). Phosphorus plays key roles in regulating plants' physiological responses to abiotic stresses. *Plants (Basel)* 12(15), 2861. doi: 10.3390/plants12152861

Kuheli, D., Vandana, K., and Reeta, G. (2003). 'P' solubilization potential of plant growth promoting *Pseudomonas* mutants at low temperature. *Microbiological Research* Vol. 158(4), 359-362. doi.org/10.1078/0944-5013-00217

Mengesha, A. S. and Legesse, N. H. (2024). Isolation and characterization of phosphate solubilizing bacteria from the rhizosphere of lentil (*Lens culinaris* M.) collected from Hagere Mariam district, Central Ethiopia. *PLoS ONE* Vol. 19(11), e0308915. doi.org/10.1371/journal. pone.0308915

Mohamed, E. A., Osama, E., Manal, E., Samah, A., Salah, G., Hazem, K. M., Jacek, W., and Nabil, E. (2021). Impact of gamma irradiation pretreatment on biochemical and molecular responses of potato growing under salt stress. *Chemical and Biological Technologies in Agriculture* Vol. 8, 35. doi.org/10.1186/s40538-021-00233-8

Pan, L. and Cai, B. (2023). Phosphate-solubilizing bacteria: advances in their physiology, molecular mechanisms and microbial community effects. *Microorganisms* 11(12), 2904. doi: 10.3390/microorganisms11122904.

Peng, Q., Xiao, Y., Zhang, S., Zhou, C., Xie, A., Li, Z., Tan, A., Zhou, L., Xie, Y., Zhao, J., Wu, C., Luo, L., Huang, J., He, T., and Sun, R. (2022). Mutation breeding of *Aspergillus niger* by atmospheric room temperature plasma to enhance phosphorus solubilization ability. *PeerJ* Vol. 10, e13076. doi: 10.7717/peerj.13076

Phua, C. K. H., Ali, T. K. Z., Chong, S. P., Mohd-Dzomir, A. Z., and Abdullah, N. H. L. (2024). Guideline on mutagenesis of biofertiliser bacteria using gamma irradiation. Agensi Nuklear Malaysia, e ISBN 978-967-2706-19-9

Phua, C. K. H., Saud, H. M., Abdul-Rahim, K., Ishak, C. F., and Wahab, P. E. M. (2019). Effects of gamma-irradiated *Acinetobacter calcoaceticus* on nitrogen and phosphorus uptake of green mustard (*Brassica chinensis*). *Malaysian Journal of Soil Science* Vol. 23, 149-166

Premono, M. E., Moawad, A. M., and Vlek, P. L. G. (1996). Effect of phosphate-solubilizing *Pseudomonas putida* on the growth of maize and its survival in the rhizosphere. *Indonesian Journal of Crop Science* 11(1), 13–23.

Sharma, D., Sharma, A., Singh, B. (2021). Effect of geometry and position of dosimeters on dose mapping of Gamma Chamber-900 using ceric-cerous dosimeter. *Journal of Radioanalytical and Nuclear Chemistry* 330, 1447–1454. DOI: 10.1007/s10967-021-07983-0

Sharmin, H., Tahsina, Deepranjan, S., Rahul, D., Mohammad, G. K., Rafi, U., Nazeer, A., Mohammad, A. H., Asim, M., and Naser A. A. (2024). Sustainable Management of Phosphorus in Agriculture for Environmental Conservation. Phosphorus in Soils and Plants. *IntechOpen* doi:10.5772/intechopen.113086

Silva, M. L. R. B., Figueirôa, C. dos S., Mergulhão, A. C. do E. S., and Lyra, M. do C. C. P. de. (2014). Diversidade e potencial de solubilização de fosfato in vitro por bactérias endofíticas associadas à cultura da palma forrageira (Opuntia e Nopalea) em Pernambuco. *Pesquisa Agropecuária Pernambucana* 43(1), 1-12. DOI: 10.12661/pap.2014.013

Solangi, F., Zhu, X., Khan, S., Rais, N., Majeed, A., Sabir, M. A., Iqbal, R., Ali, S., Hafeez, A., Ali, B., Ercisli, S., and Kayabasi, E. T. (2023). The global dilemma of soil legacy phosphorus and its improvement strategies under recent changes in agro-ecosystem sustainability. *ACS Omega* Vol. 8(26), 23271-23282. doi: 10.1021/acsomega.3c00823

Wakako, S., Masayuki, S., Kyoko, M., and Masaaki, M. (2014). Plant growth-promoting bacterium *Acinetobacter calcoaceticus* P23 increases the chlorophyll content of the monocot Lemna minor (duckweed) and the dicot *Lactuca sativa* (lettuce). *Journal of Bioscience and Bioengineering* Vol. 118 (1), 41-44. doi.org/10.1016/j.jbiosc.2013.12.007

Yang, T., Li, L., Wang, B., Tian, J., Shi, F., Zhang, S., and Wu, Z. (2022). Isolation, mutagenesis, and organic acid secretion of a highly efficient phosphate-solubilizing fungus. *Frontiers in Microbiology* Vol. 13, 793122. doi: 10.3389/fmicb.2022.793122

Zhang, T., Jian, Q., Yao, X., Guan, L., Li, L., Liu, F., Zhang, C., Li, D., Tang, H., and Lu, L. (2024). Plant growth-promoting rhizobacteria (PGPR) improve the growth and quality of several crops. *Heliyon* Vol. 10(10). doi.org/10.1016/j.heliyon.2024.e31553